

Onset of Vortex Shedding and Hysteresis in Flow over Tandem Sharp-Edged Cylinders of Diverse Cross Sections

M. Kouchakzad¹, A. Sohankar^{2,*}, M.R. Rastan^{3,†}

¹ Mechanical Engineering Group, Pardis College, Isfahan University of Technology, Isfahan, 84156-83111, Iran

² Department of Mechanical Engineering, Isfahan University of Technology, Isfahan, 84156-83111, Iran

³ Department of Engineering Mechanics, School of Naval Architecture, Ocean and Civil Engineering, Shanghai Jiao Tong University, 200240, Shanghai, China

[†] Email: rastan@sjtu.edu.cn

Abstract

Numerical simulations are conducted to analyze flow characteristics around two tandem sharp-edged cylinders with cross sections of square ($b_1^* = 1$) for the upstream cylinder and rectangle (b_2^*) for the downstream cylinder ($b^* = b/a$, where a and b are the sides of cylinders). The study investigates the effects of Reynolds numbers ($Re = 30-150$), cross-sectional aspect ratios of the downstream cylinder ($b_2^* = 1 - 4$), and scaled gap-spacing between cylinders ($S^* = 1-6$) on the flow structure, onset of vortex shedding, hysteresis and aerodynamic parameters. The results reveal that increasing b_2^* suppresses the vortex shedding of the upstream cylinder, depending on S^* . The suppression is attributed to the interference effect and the adhesion of the shear layers on the downstream cylinder. Three distinct time-mean flow patterns are identified based on the separation and reattachment of shear layers. Flow pattern *I* exhibits parallel flow along the side faces of the upstream cylinder, while the separation bubbles associated with reattachment points are formed in flow pattern *II* on these faces. For pattern *III*, no reattachment point is observed and the separation bubbles cover the upstream cylinder' side faces. Additionally, two instantaneous flow patterns of extended-body and co-shedding are apperceived within the ranges of examined Re and S^* . The behaviors of time-mean and varying forces as well as the vortex shedding frequency are correlated with the flow structures. The onset of vortex shedding and hysteresis dependence are discussed comprehensively. The results show that the critical Reynolds numbers for the onset of vortex shedding decrease from 128 ± 2 to 50 ± 2 with S^* increasing from 1 to 6 ($b_1^* = 1$ and $b_2^* = 4$). The hysteresis limit is found within the range of $3.5 \leq S^* \leq 4.5$ for flow over two tandem cylinders ($b_1^* = 1$ and $b_2^* = 4$) at $Re = 150$.

Keywords: Tandem sharp-edged cylinders; Mean and instantaneous flow patterns; Onset of vortex shedding; Hysteresis; Numerical study.

1. Introduction

Given the importance of the flow over circular and prismatic bluff bodies practically and fundamentally, it is still an active topic although classic. The applications span heat exchangers, coastal structures, and cables at high Reynolds numbers ($Re = U_{in}a/v$, where U_{in} and “ a ” denote freestream velocity and side length) and electronic chips and mini or micro-devices at low- Re , to name a few. The complex flow phenomena such as flow separation and reattachment, shear layer

and wake instability, and vortex shedding have been investigated widely for 2D and 3D square/circular cylinders in different arrangements (e.g., tandem, side-by-side, staggered) [1-8] and isolated/single ones [9-16]. Although the cross-section significance has been documented already [17], the studies on tandem cylinders mostly focused on twin circular and square ones due to widespread applications and simplicity for flow physics assimilation. The rectangular cross-section and the arrangement of non-homogeneous structures are also omnipresent in human-designed systems; however, they have not yet received the attention that they deserve.

The flow around single or tandem square cylinders is fully attached with no separation at $Re \approx 1$. The steady/laminar flow starts to separate at $Re \approx 5$, generating two symmetric/steady recirculation bubbles behind the cylinders [18]. The bubble size is enlarged monotonically with a Re increment till a critical Re (i.e. Re_{cr}) in which the vortex shedding starts. The two streets of oppositely-signed convective spanwise vortices (i.e., vortex shedding) cause oscillatory drag and lift forces on the cylinder. A Re increase augments the amplitudes of the oscillatory force components. Locating an obstacle in the wake of the preliminary prism changes the above scenario entirely. The flow patterns are not simply a function of Re , but also gap spacing and the configuration of the downstream prism [19]. For instance, the aerodynamic force unsteadiness and onset of vortex shedding occurs at $Re_{cr} = 45 - 55$ at $S^* = 5$ [18] and $Re_{cr} = 60 - 65$ at $S^* = 4$ [20] for two tandem square cylinders. The corresponding critical Re values for the circular counterpart are $Re_{cr} = 75.5$ and 68 at $S^* = 2$ and 4 , respectively [1, 21]. It should be noted that the range of the critical Reynolds number or vortex shedding for two tandem rectangular cylinders has not been reported so far. Rastan and Alam [19] thoroughly discussed the flow transition and flow pattern dependence for two tandem circular and square cylinders in $S^* \leq 9$ and $Re < 10^5$. They reported that the flow interference between two cylinders is susceptible to stabilizing the flow with $S^* < S^*_{cr}$, where S^*_{cr} is a critical spacing for the onset of the co-shedding flow regime between the cylinders.

Table 1 lists, the experimental and numerical studies on two tandem square/rectangular cylinders. In this table, the range of Reynolds numbers, cylinder gap-spacing (S^*), hysteresis limit, and research findings are presented. This table clarifies that the studies on two tandem sharp-edged cylinders at low Reynolds numbers and the onset of vortex shedding are very limited. Therefore, this study investigates the effect of cylinder gap-spacing and aspect ratio of downstream cylinder on the onset of vortex shedding for two tandem sharp-edged cylinders with different sections.

The three extended/slender-body flow, alternating reattachment flow and co-shedding flow regimes emerge over the tandem cylinders and their occurrence is a function of the S^* and Re values [17-26]. Some researchers reported a fourth regime called bistable flow with a systematic increase in the S^* at high Reynolds numbers of $9.7 \times 10^3 - 6.5 \times 10^4$ [19]. The bistable flow, intermittently swings between two between alternating reattachment and co-shedding flow regimes. For extended/slender-body flow regimes, the upstream-cylinder-generated shear layers either originate at the trailing corners and almost steadily attach to the downstream cylinder at low- Re flows or separate at leading corners and overshoot the downstream cylinder at high- Re flows. The vortices shed only in the wake of the downstream cylinder and a pair of symmetrical bubbles is formed in the gap region. For the reattachment flow, the upstream-cylinder-generated

shear layers reattach either side of the downstream cylinder alternatively, while no vortex shedding is seen in the gap. Due to the alternate reattachment, the gap bubbles are asymmetrical. The co-shedding flow regime is characterized by the vortex shedding from both cylinders.

Table 1. A summary of studies on the flow over two tandem square cylinders (except [17, 35], i.e. tandem rectangular cylinders), where Num. and Exp. stand for the numerical and experimental methods. S^* : Scaled gap spacing; OVS : Onset of vortex shedding; HL : Hysteresis limit; St : Strouhal number; GP : Global parameters.

Ref.	Method	Re	S^*	HL	Findings
Sohankar et al. [2]	Exp.	2033	1-6	-	St , GP
Liu et al. [17]	Num.	150	1-8	-	St , GP
Sohankar and Etmnan [18]	Num.	1 – 200	5	-	OVS , St , GP
Rastan and Alam [19]	Num.	$Re < 10^5$	1.5-7	4.5-7	St , GP
Sohankar [20]	Num.	$40 - 1 \times 10^3$	0.3-12	2.75-4.75	St , GP
Liu and Chen [22]	Exp.	$2 \times 10^3 - 1.6 \times 10^4$	1.5-9	2.5-4.25	OVS , St , GP
Sohankar et al. [23]	Num.	70 – 150	1-5	2-5	St , GP
Sobczyk et al. [24]	Exp.	$4.1 \times 10^3 - 3.294 \times 10^4$	2-9	3-8.6	St , GP
Sohankar [25]	Num.	$1 \times 10^3 - 1 \times 10^5$	1-12	2.25-4.25	St , GP
Nikfarjam and Sohankar [26]	Num.	100 – 150	1-8	3.5-4.5	St , GP
Kim et al. [27]	Exp.	$5.3 \times 10^3 - 1.6 \times 10^4$	1.5-11	-	St , GP
Yen et al. [28]	Exp.	$300 - 1.1 \times 10^3$	1.5-3.5	-	St , GP
Nikfarjam and Sohankar [29]	Num.	40 – 160	4	-	GP
Xiaiqing et al. [30]	Exp.	8×10^4	1.25-5	-	GP
Shao et al. [31]	Num.	100	2-6	-	St , GP
Kumar et al. [32]	Num.	40	2-30	-	St , GP
Shang et al. [33]	Num.	5.3×10^3	4	-	St , GP
Shui et al. [34]	Num.	100	1.5-9	-	GP
Islam et al. [35]	Num.	75-150	0.5-10	-	St , GP

The flow regime is highly correlated with the engineering parameters such as aerodynamic forces and vortex shedding frequency (i.e. Strouhal number). Therefore, understanding how the flow regime varies with S^* and Re is worthwhile. For example, it has been well-documented that the flow modification from the attachment flow regime to the co-shedding regime is accompanied by an abrupt change in both St and fluid force. However, shifting from one flow regime to another is not that straightforward due to hysteresis, where the aerodynamic specifications are highly dependent on the flow history. This phenomenon for the twin tandem cylinders is observed in a specific range of gap spacing (i.e., hysteresis limit or HL , see Table 1) [19, 20, 22-26]. In other words, the flow regime in a given S^* and Re is contingent on the past flow state, e.g., varying the gap spacing either in a progressively increasing or decreasing manner. Table 1 illustrates hysteresis pops up in $2.5 \leq HL \leq 7$ if the downstream cylinder is displaced so slowly, regardless of Reynolds numbers [19, 20, 22-26]. Sobczyk et al. [24] observed the range shrinks to $HL = 3.0 - 6.8$ at $Re = 4100 - 32940$ if the downstream cylinder is displaced a bit faster (speed of 0.09 in their study).

Among the studies in Table 1, only Islam et al. [35] and Liu et al. [17] took into consideration the tandem rectangular cylinders; no study has been reported on the sharp-edged tandem cylinders with non-identical cross-section. Islam et al. [35] examined the effect of $b^* = 0.25 - 1.0$,

$S^* = 0.5 - 10$, and $Re = 75 - 150$ on the results ($b^* = b/a$, where a and b are the sides of cylinders). Their findings show that the upstream cylinder has a higher drag force compared to that of the downstream cylinder. According to aspect ratio variation, several flow regimes were identified. In unsteady regimes, they found more than one peak in the power spectra of the downstream cylinder. It was reported that the vortex shedding mostly occurs behind the downstream cylinder and the root mean square (RMS) of the lift coefficient for the upstream cylinder is considerably lower than that of the downstream cylinder. Liu et al. [17] also investigated a similar configuration ($b^* = 0.3 - 4$, $S^* = 1 - 8$) at $Re = 150$. The flow patterns were categorized by S^* as a narrow gap ($S^* = 1.0, 2.0$), medium gap ($S^* = 3.0, 4.0$), and wide gap ($S^* = 6.0, 8.0$). It was also found that a larger b^* reduces the fluctuating force acting on the downstream cylinder for narrow gaps, but amplifies for wide gaps. The findings show the narrow gap suppresses the vortex shedding of the upstream cylinder; the aspect ratio has less effect on the fluid force of the two tandem cylinders. Furthermore, the vortex shedding of the downstream cylinder diminishes by increasing b^* . They reported that the fluid forces of the downstream cylinder for a wide gap are more dependent on b^* , compared to cases with a narrow gap.

Despite some studies on two tandem square [18-20, 22-34] and rectangular [17, 35] cylinders (see Table 1), the above literature review illustrates that the flow around two tandem sharp-edged cylinders with non-similar cross-sections has yet to be investigated. On the other hand, assimilating complex phenomena such as hysteresis [36] and the onset of vortex shedding motivates us to perform low Re simulations. Studying low Re flows is common to dispel unanticipated challenges in the path of developing novel approaches (e.g., [37]) and to generalize the concepts to high Reynolds numbers flows (e.g., [38,39]). Therefore, $Re = 30-150$ and $S^* = 1-6$, $b_1^* = 1$ and $b_2^* = 1 - 4$ are selected to fill the knowledge gap. The specific objectives of this study are (i) illustrating the critical parameters associated with the onset of vortex shedding, (ii) categorizing the flow patterns and correlating them with the engineering parameters, (iii) and eventually, determining the hysteresis limit, and detailing the dependence of the aerodynamic forces on this phenomenon. To this end, the Strouhal number, fluctuating lift and drag coefficients, pressure coefficient, fluctuating normal and shear stresses, and flow patterns are scrutinized in this study.

2. Problem definition and formulation

Figure 1 schematically shows the computational domain of the problem under consideration. A rectangle ($b_2^* = 1 - 4$) prism (Cyl2) is arranged in tandem behind a square ($a = b$ or $b_1^* = 1$) one (Cyl1). The dimensions are scaled with “ a ”, and denoted with “*” superscript (e.g., $L_1^* = L_1/a$). Table 2 compares the Re , S^* , computational domain size, and blockage ratio $\beta = a/h$ between current and previous (two tandem square cylinders) studies. It has been well-documented [9,18] that $\beta \leq 5\%$ is mandatory for keeping the computational results independent of the lateral boundaries’ location. $L_1^* = 10$, $L_2^* = 20$, $h^* = 20$, and $S^* = 1 - 6$ were chosen for this study; thus, $\beta = 5\%$.

Table 2. Comparison of the computational domain size (see also Fig. 1) between current and previous (two tandem square cylinders) studies.

Ref.	Re	S^*	L_1^*	L_2^*	h^*	$\beta(\%)$	2D/3D
Sohankar et al. [18]	1-200	5	5	15	20	5	2D
Rastan et al. [19]	$Re < 10^5$	1.5-7	10	25	20	5	2D-3D
Sohankar [20]	40-1000	0.3-12	7	16	20	5	2D-3D
Sohankar et al. [23]	70-150	1-5	10	25	20	5	2D
Sohankar [25]	$10^3 - 10^5$	1-12	8	16	20	5	3D
Nikfarjam et al. [26]	100-150	1-8	8.5	16.5	20	5	2D
Nikfarjam et al. [29]	100-160	4	8.5	16.5	20	5	2D
Shui et al. [34]	100	1.5-9	4	21.5	18	5.5	2D
Present	30-150	1-6	10	20	20	5	2D

The time-dependent continuity and momentum equations in Eqs. 1 – 2 govern the laminar flow motion in the present study. Dealing with the two-dimensional incompressible flow with constant properties in a Cartesian coordinate system, they are expressed as follows:

$$U_{i,i}^* = 0 \quad (1)$$

$$U_{i,\tau}^* + (U_i^* U_j^*)_{,j} = -P_{,i}^* + Re^{-1} U_{i,jj}^* \quad i, j = 1, 2 \quad (2)$$

U^* and P^* are scaled velocity and pressure. The pressure, time, and velocity have been made dimensionless using ρU_{in}^2 (ρ fluid density), a/U_{in} , and U_{in} , respectively. The drag coefficient, C_d , lift coefficient C_l , friction coefficient C_f , pressure coefficient C_p , and Strouhal number St are defined in Eq. 3.

$$C_d = \frac{F_d}{0.5\rho U_{in}^2 a}, \quad C_l = \frac{F_L}{0.5\rho U_{in}^2 a}, \quad C_f = \frac{\tau_s}{0.5\rho U_{in}^2}, \quad C_p = \frac{P - P_\infty}{0.5\rho U_{in}^2}, \quad St = \frac{fa}{U_{in}} \quad (3)$$

The f , F_d , F_L , and P_∞ are, respectively, the vortex shedding frequency, drag force, lift force, and freestream pressure. The τ_s is the wall shear stress. The RMS of lift and drag coefficients are provided in Eq. 4.

$$C_{l,rms} = \sqrt{\frac{1}{N} \sum_1^N (C_l(t) - \bar{C}_l)^2} \quad C_{d,rms} = \sqrt{\frac{1}{N} \sum_1^N (C_d(t) - \bar{C}_d)^2} \quad (4)$$

The governing equations are numerically solved in a finite volume context using Ansys-Fluent 2019. The diffusion term is discretized by second-order central differencing. The convective term is discretized by Quick's method, which is based on the weighted average of second-order-upwind and central interpolations of the variable. The second-order implicit method is also applied for temporal discretization. The Semi-Implicit Method for Pressure-Linked Equations

(SIMPLE) scheme deals with pressure-velocity coupling. The time-marching is performed by steps of 0.02 (see Table 3) and the residual values or convergence criteria for all quantities are set to 10^{-5} .

A uniform flow is imposed in the x-direction at the inlet. While the zero-gradient velocity sets the outlet of the computational domain. For solid surfaces, the no-slip condition is used. The top and bottom boundaries are modeled as free-slip boundaries, which impose zero normal velocity and zero shear stress. The boundary conditions are summarized as (see also Fig. 1):

$$\begin{aligned} \text{Inlet boundary: } u^* = 1, v^* = 0, & \quad \text{Outlet boundary: } \frac{\partial v^*}{\partial x^*} = \frac{\partial u^*}{\partial x^*} = 0 \\ \text{Side boundary: } v^* = \frac{\partial u^*}{\partial y^*} = 0, & \quad \text{Cylinders surface: } u^* = v^* = 0, \end{aligned}$$

3. Validation and grid/time step independence study

The grids with structured tetrahedral cells and non-uniform node spacing were generated. Those next to the solid boundaries (i.e. δ^* the first grid distance from the cylinder surface) are gradually enlarged with a stretching ratio of less than 1.02 up to 5a in every direction, except 10a, behind the downstream cylinder. The grid size from the middle of the gap spacing shrinks towards the cylinders at a rate of less than 1.05. Further away from this non-uniform grid area, the largest cells (i.e. Δ^*) spatially discretize the computational domain. Figure 2 shows a typical grid generated for the case with $b_1^* = 1$, $b_2^* = 4$, and $S^* = 4$.

If N_a and N_b are respectively the numbers of nodes on the longitudinal sides of Cyl1 and Cyl2, the $N_a = 40$ and $N_b = 60, 70, 80$ for $b_2^* = 2, 3$, and 4 are considered. Furthermore, the number of gap nodes in the x-direction increases as $N_{dis} = 40, 60, 70, 80, 90$, and 100 for $S^* = 1 - 6$ with step one, respectively. To find other specifications for the proper grids, a study was performed for $b_2^* = 4$ by comparing the smallest (δ^*) and largest (Δ^*) grid cell, number of nodes in x (N_x) and y (N_y) direction and global parameters (i.e., St , \bar{C}_d , C_{lrms}), see Table 3. This table also presents the study of time step influence at $Re = 150$ for a given grid. Except for grids 1 and 2, the results from different grids agree well with each other. The results of grid 4 (71984 nodes) are almost unchanged compared to grids 5 (75856 nodes) and 6 (92700 nodes). Moreover, the hysteresis range was checked with grid numbers 4 and 6. It was observed that both meshes specify the hysteresis limit with the same accuracy. The time step size influence on the results was also examined by studying $\Delta_t^* = 0.01, 0.02$, and 0.03 (see Table 3). The variation of St and C_{lrms} with $\Delta_t^* = 0.02$ and 0.01 are insignificant. However, increasing Δ_t^* to 0.03 leads to a $\sim 15\%$ discrepancy in \bar{C}_d of Cyl2. Given this examination, $\Delta_t^* = 0.02$ was considered for all simulations.

Table 3. Grid and time step independence tests for the case with $b_1^* = 1$, $b_2^* = 4$, $S^* = 4$, $Re = 100, 150$. N_x and N_y are the node numbers in the x and y direction, and Δ_t^* shows the scaled time step.

Grid	Re	$S^* = 4$				Cyl1		Cyl2		
		δ^*	Δ^*	$N_x * N_y$	Δ_t^*	St	\bar{C}_d	St	\bar{C}_d	C_{lrms}
1	100	0.015	0.3	320*118	0.02	0.120	1.309	0.120	1.029	0.066
2	100	0.01	0.25	351*150	0.02	0.119	1.290	0.118	1.005	0.052
3	100	0.007	0.25	388*176	0.02	0.112	1.287	0.112	0.199	0.052
4	100	0.007	0.25	409*176	0.02	0.112	1.280	0.112	0.199	0.051
5	100	0.005	0.2	431*176	0.02	0.112	1.280	0.112	0.199	0.051
6	100	0.005	0.18	450*206	0.02	0.112	1.280	0.112	0.199	0.051
5	150	0.005	0.2	431*176	0.02	0.120	1.428	0.120	-0.028	0.100
6	150	0.005	0.18	450*206	0.02	0.120	1.427	0.120	-0.028	0.100
4	150	0.007	0.25	409*176	0.01	0.120	1.428	0.120	-0.028	0.100
4	150	0.007	0.25	409*176	0.02	0.120	1.428	0.120	-0.028	0.100
4	150	0.007	0.25	409*176	0.03	0.121	1.410	0.121	-0.024	0.101

For further grid inspection, the surface pressure coefficient and the mean velocity on the centerline ($y = 0$) are compared at $Re = 150$ for grids in Table 3. Although a satisfactory agreement between \bar{C}_p profiles is seen for Cyl1 in Fig. 3a, grid 1 shows a maximum 61% discrepancy for Cyl2, compared with those of grids 3-6 in Fig. 3b. At $x > 15$ the u_{avr} on the center line ($y = 0$) for grids 1 and 2 compared to those of grids 3-6 have maximum differences about 50% and 17%, respectively. While it is the same for $x < 15$ (Fig. 3 c). In other words, the local characteristics (i.e. \bar{C}_p) and mean parameters (i.e. u_{avr}) for grid 3-6 are independent of the grid number. Therefore, grid 4 was chosen to keep the accuracy and optimize the computation time. Grid 4 specifications (e.g. expansion ratio and the smallest cell size) are used to generate the grids of other b_2^* values.

Due to the lack of appropriate data for verification, Fig. 3 compares the \bar{C}_d of tandem square cylinders at different S^* and $Re = 150$ with the previous attempts [17, 20, 26] for validation purposes. Aerodynamic parameters such as drag coefficient are bifurcated in the cylinder gap-spacing $S^* = 2-5$, which shows the effect of hysteresis on the flow (Fig. 3 (d, e)). The results have good compliance (mostly less than 3.5%) with previous studies in the hysteresis limit (mode1 & mode2).

Table 4 compares (a) the results of flow over a single square cylinder and (b) two tandem square cylinders with $S^* = 4$ at $Re = 100$ & 150 with available data in the literature. This comparison shows that the global results for a single cylinder are in good agreement (mainly less than 8% for C_{lrms} and 5% for other parameters) with those of previous works. Moreover, flow over two

tandem square cylinders ($Re = 100$ - Table 4 (b)) is also compared with the reported results of flow over tandem square cylinders [20, 26]. The results are in good agreement (the percentage deviation less than 3%) with the previous studies.

Table 4. Comparison of our results with previous publications for (a) a single square cylinder and (b) two tandem square cylinders with $b_1^* = b_2^* = 1$ ($Re = 100, 150$).

(a)	Ref.	Re	\overline{C}_d (Max difference)	St (Max difference)	C_{drms} (Max difference)	C_{brms} (Max difference)
	Mashhadi et al [14]	100	1.503	0.148	0.008 (2.1%)	0.184
	Sohankar et al [18]	100	1.533 (2.6%)	0.149	0.007	0.204 (7.9%)
	Sharma et al. [40]	100	1.495	0.148	0.006	0.192 (1.5%)
	Sen et al [41]	100	1.530	0.145 (1.4%)	-	0.193
	Present	100	1.493	0.147	0.0054	0.189
	Aboueian et al. [3]	150	1.453	0.158	0.0156	0.264 (8.3%)
	Mashhadi et al [14]	150	1.466	0.162	0.017 (4.2%)	0.269
	Sharma et al. [40]	150	1.465	0.158	0.016	0.291
	Zheng and Alam [42]	150	1.483	0.158	0.0163	0.277
	Alam et al [43]	150	1.492 (3.1%)	0.154 (3.1%)	0.0155 (5%)	0.271
	Present	150	1.447	0.159	0.0163	0.288

(b)	Ref.	$S^* = 4$ Re	St	Cyl1($b_1^* = 1$) \overline{C}_d	Cyl2($b_2^* = 1$) \overline{C}_d
	Sohankar et al. [20]	100	0.139 (2.2%)	1.472 (0.9%)	1.178 (2.7%)
	Nikfarjam et al. [26]	100	0.135 (0.8%)	1.434 (2.3%)	1.138 (0.8%)
	Present	100	0.136	1.458	1.147

4. Results and discussion

Numerical simulations are performed at $Re = 30-150$ and $S^* = 1-6$ to study gap and wake flows of square ($b_1^* = 1$) and rectangle ($b_2^* = 1 - 4$) prisms in a tandem arrangement. The critical Reynolds number (Re_{cr}) associated with the transition from steady to unsteady flow is determined first. Then, the flow patterns are categorized and the engineering parameters, such as aerodynamic force and shedding frequency, are discussed thoroughly. Finally, the hysteresis at $Re = 150$ is scrutinized.

4-1 Onset of vortex shedding (Re_{cr})

4-1-1 Re_{cr} for various S^* ($b_1^* = 1, b_2^* = 4$)

The flow is steady when the Re is less than a critical one. As such, there are no fluctuations in lift and drag signals. Figure 4 (a, b) shows the lift and drag coefficients at $Re = 70, S^* = 5$, and, $b_2^* = 4$, where no fluctuation is observed. The flow is thus steady at $Re \leq 70$ for $S^* = 5$. Oscillating the lift and drag coefficients for both cylinders at $Re = 75$ is periodic (Fig. 4 (b, c)), which is a signature of unsteady flow and shedding the vortices. As a result, the onset of vortex shedding for $S^* = 5$ transpires at $70 < Re < 75$.

With a similar approach to determine the Re_{cr} range, Fig. 4 depicts the vortex shedding inception threshold for various S^* or b_2^* values. Given the uncertainty of this method (e, g. $70 < Re_{cr} < 75$),

the mid-value has been assumed to serve as Re_{cr} , e.g., $Re_{cr} = 73 \pm 2$ for $S^* = 5$, $b_1^* = 1$, $b_2^* = 4$ (see Fig. 4). Figure 5 (a) illustrates the Re_{cr} ($S^* = 1 - 6$, $b_1^* = 1$, $b_2^* = 4$). But the vortices do not shed necessarily from the upstream cylinder at Re between 30 to 150 and $S^* = 1 - 4$. While it is the case for $S^* = 5, 6$ and the Re_{cr} is the same for both cylinders. Nonetheless, with a focus on the shedding in the wake of the downstream cylinder, the $Re_{cr} = 128 \pm 2$, 119 ± 2 , 113 ± 2 , 93 ± 2 , 73 ± 2 , 50 ± 2 for $S^* = 1, 2, 3, 4, 5, 6$, respectively.

The Re_{cr} at $S^* = 6$ approaches that of a single square cylinder with $Re_{cr} = 51.2$ [9]. This observation is ascribed to the mitigation of the interference effect, where the cylinder in the wake of another at higher S^* behaves as an isolated obstacle. The results in Fig. 5 (a, b) are fitted with a curve, and corresponding relations are presented in Eqs. 6 and 7. Eq. 6 is valid for the downstream cylinder, irrespective of S^* , but only for the upstream cylinder at $S^* = 5, 6$. Eq. 7 represents the Re_{cr} for $b_2^* = 1 - 4$. The deviation between the data and curve fits at Eqs. 6 and 7 is less than 3% and 0.5%, respectively.

$$Re_{cr} = 131.4 - 1.185S^* - 2.0714 S^{*2} \quad (6)$$

$$Re_{cr} = -191 + 385b_2^* - 128.5 b_2^{*2} + 12.5 b_2^{*3} \quad (7)$$

4-1-2 Re_{cr} for various b_2^* ($S^* = 4$, $b_1^* = 1$)

This section reports the Re_{cr} values for $S^* = 4$ and various b_2^* . Fig. 5 (b) shows $Re_{cr} = 78 \pm 2$ for both cylinders when $b_1^* = b_2^* = 1$. This Re_{cr} concurs well with 80 ± 10 from Ref. [19]. The vortices do not shed from the upstream cylinder but it occurs for the downstream cylinder with b_2^* of 2 - 4 ($S^* = 4$, $b_1^* = 1$). Thus, an increase of b_2^* ceases the upstream cylinder vortex shedding. The critical Reynolds numbers for the downstream cylinder are $Re_{cr} = 165 \pm 2$, 145 ± 2 , 93 ± 2 for $b_2^* = 2, 3, 4$, respectively. This figure also reveals that the Re_{cr} increases with the b_2^* increment from 1 to 2, and then decreases. Therefore, at a fixed S^* , the onset of the vortex shedding is postponed first by increasing b_2^* , and then approaches that of equal tandem cylinders. In other words, adding a cylinder in the wake of another controls the upstream cylinder wake and suppresses or delays the vortex shedding. It is worth noting that 140 unsteady simulations for various Re , S^* , and b_2^* were performed to find the Re_{cr} .

4-2 Flow patterns

4-2-1 Instantaneous flow pattern

The identification of vortex can be carried out by analyzing the streamlines, contours of vorticity, and Q (Figs. 6 and 7). The Q criterion defines the vortex core as a continuous region with a positive second invariant (∇u) [44, 45]. It should be emphasized that the Q criterion and vorticity provide relatively similar vortex cores for 2D simulations; thus, the streamlines and contours of vorticity are mostly discussed. Figure 6 shows the streamlines and vorticity contours (ω_z^* , scaled by "a" and U_{in}) at an instant in which the lift coefficient is maximum. Beyond the zones in which the flow is steady or $Re > Re_{cr}$, two distinct flow patterns of the extended-body (EBF) and co-

shedding (*CSF*) are found as shown in Fig. 6. For the former (*EBF*), the upstream-cylinder-generated shear layers steadily glide on the downstream cylinder, separate from its trailing edges, roll up in the wake alternatively and form a single vortex street behind the downstream cylinder, see Fig. 6 (a-d, i, j). For the latter (*CSF*), the upstream-cylinder-generated shear layers transform into vortices and shed alternately in the gap (Fig. 6 (e, f, g)). Vortex shedding occurs behind both cylinders in this case.

The steady flow was observed at $S^* = 1-6$ and $Re < Re_{cr}$, e.g. see Fig. 6 (h). The extended-body flow occurs for $S^* < 5$ and $75 \leq Re \leq 150$ at $b_2^* = 4$. This flow pattern is seen when the gap spacing is less than a critical value, i.e., $S^* < S_{cr}^*$. A pair of symmetric vortices are formed between two cylinders for $S^* \leq 4$ ($b_2^* = 4$) and no vortex sheds from the upstream cylinder. While the vortex shedding is observed at $Re > Re_{cr}$ behind the downstream cylinder. The reattachment flow pattern is not observed at $S^* = 5, 6$ for $Re > Re_{cr}$. The critical gap spacing is between 4 and 5 for $b_2^* = 4$. Beyond that, the co-shedding flow is observed at $Re = 75-150$ for $S^* \geq 5$ and $Re = 55-150$ for $S^* \geq 6$.

The previous studies for tandem square cylinders ($b_1^* = b_2^* = 1$) widely reported the alternating reattachment flow at a certain range of S^* [18, 19, 22]. This flow pattern is not observed in this study, and the flow pattern transits from extended-body flow to co-shedding directly (Fig. 6). The rectangle cross-section ($b_2^* = 4$) of the downstream cylinder likely modulates the alternation of the upstream cylinder-generated shear layers and ceases the swinging motion of reattachment points on the lateral cylinder faces. Because of the same reason, the two gap bubbles are steadily identical. Whereas, the asymmetry of these bubbles has been reported [19] for the reattachment flows for the twin tandem cylinders.

For a given gap spacing of $S^* = 4$, the flow structure dependence on $b_2^* = 1 - 4$ is discussed here. As mentioned, the flow is steady at $Re < Re_{cr}$, e.g. for $b_2^* = 1 - 4$ ($S^* = 4$). The results show that the co-shedding flow emerges for $b_1^* = b_2^* = 1$ at $Re_{cr} \leq Re \leq 150$ (Fig. 6g), while the extended-body flow occurs for $b_1^* = 1, b_2^* = 3 - 4$ at $Re_{cr} \leq Re \leq 150$ (Fig. 6(i, j)). Interestingly, the flow over both cylinders remains steady at $b_2^* = 2$ up to $Re = 160$ (see Fig. 6h), i.e., the vortex shedding associated with the extended-body flow is postponed up to $Re_{cr} \geq 165 \pm 2$. The alternating reattachment flow was not observed for any cases ($S^* = 4, b_1^* = 1, b_2^* = 1 - 4, Re \leq 150$).

The values of vorticity at the center of vortices are also shown in Fig. 6 (g-j) for $Re = 150$, which decreases along the streamwise. Moreover, Fig. 6 (g, h) illustrates that the flow is unsteady at $b_2^* = 1$ and steady at $b_2^* = 2$. Whereas, the gap flow is quasi-steady at $b^* = 3$ and 4. The result shows that the co-shedding flow occurs for $Re > 75$ at $b_1^* = b_2^* = 1$ (e.g. see Fig. 6 (g)), but not anymore for $b_2^* > 1$ at any given Re up to 150 ($Re_{cr} = 165 \pm 2$). It means that increasing b_2^* suppresses the vortex shedding from both cylinders at $b_2^* = 2$ (e.g. at $Re = 150$, Fig. 6 (h)), and then the extended-body flow pattern pops up for $b_2^* = 3, 4$ at $Re \geq 140, 90$, respectively.

Figure 7 (a,b) shows the maximum vorticity magnitude $|\omega_z^*|_{max}$ of the detached vortices (identified by Q-criterion in Fig. 7 (c,d)) behind the downstream (Cyl2) and upstream (Cyl1) cylinders, available for both of them in the co-shedding flow and only for the downstream one in

the extended-body flow. For the extended-body flow ($S^* \leq 4$), the $|\omega_z^*|_{max}$ values are almost constant irrespective of S^* but they sharply increase at $4 < S^* \leq 5$ by transforming the flow patterns to co-shedding flow (Fig. 7 (a)). For $S^* \geq 5$, the $|\omega_z^*|_{max}$ values slightly decrease for both cylinders (Fig. 7 (a)). A sudden drop in the $|\omega_z^*|_{max}$ of the downstream cylinder is observed in Fig. 7(b) with increasing b_2^* from 1 to 2. This variation is also attributed to the flow pattern change, but in this case from co-shedding to steady flow, see also Fig. 6 (g, h). Then the $|\omega_z^*|_{max}$ has a small variation with increasing b_2^* from 2 to 4, where the extended-body flow occurs (see Fig. 6 (i, j)).

The instantaneous results are reported in Fig. 6 only for $Re=150$. To find mean/instantaneous flow patterns and global parameters for various Re , S^* , and b_2^* , many unsteady simulations are carried out for $Re = 30-150$, $S^* = 1 - 6$, and $b_2^* = 1 - 4$. All simulations performed for various Re and S^* ($b_2^* = 4$, $b_1^* = 1$) and Re and b_2^* ($S^* = 4$, $b_1^* = 1$) are shown in Figs. 8 a and b, respectively. In this $Re - S^*$ or $Re - b_2^*$ plane, the squares specify simulated cases and the gray and yellow regions illustrate the extended-body (*EBF*) and co-shedding (*CSF*) flow patterns, respectively. The green line in this figure shows the positions of Re_{cr} for each S^* or b_2^* , where this boundary separates the steady and unsteady (including both *EBF* and *CSF* regions) flow zones. These flow maps show a comprehensive overview of all steady/unsteady flow patterns that occur for each Re , S^* and b_2^* .

4-2-2 Mean flow patterns

Figures 9 and 10 show the time-mean flows at $b_1^* = 1$ and $b_2^* = 4$ for various Re and S^* . Due to the elongation of the downstream cylinder ($b_2^* = 4$), the mean streamlines around the downstream cylinder are almost the same regardless of Re and S^* values. Therefore, the mean flow patterns are categorized according to the separation and reconnection on the upstream cylinder. It should be noted that the instantaneous (Fig. 8 (a)) and mean flow patterns (Fig. 9 (a)) regions around the critical Reynolds numbers overlap with each other. The Re_{cr} lines in this figure separate the steady and unsteady flow zones. The blue squares in Fig. 9 (a) specify the simulated cases and the three time-mean flow patterns are named *I*, *II*, *III*. The variation of time-mean flow characteristics such as separation and reattachment points with Re , b_2^* , and S^* are investigated in this investigation. The separation (*SP*), reattachment (*RP*), and saddle (*SD*) points are marked in Fig. 9 (b-d). Some parameters are defined in Fig. 10(a,d) for quantifying the time-mean flow features, including the gap and wake bubble lengths L_r^* and widths W_r^* , the side bubble length L_s^* , the separation point location L_d^* , and the side bubble width W_s^* . It should be noted that all lengths are scaled with “a”, see Fig. 1.

Mean flow pattern *I* show no reattachment or separation bubble on the side faces of both cylinders and the streamlines are parallel to them. The mean flow is separated from the cylinders’ rear corners (*RC*) and a pair of recirculation bubbles form in both gap and wake regions (Fig. 9 (b)). For example, this flow pattern is observed in the range of $Re = 30-95$ at $S^* = 1 - 4$ ($b_2^* = 4$), see Table 5 and Fig. 10 (a) for more details. It should be emphasized that Table 5 lists the data from Fig. 10 for $b_1^* = 1$, $b_2^* = 4$, and $S^* = 4$ in $Re = 30-150$.

Flow separates from the leading corners (*FC*) of the upstream cylinder in pattern *II*, reattaches on the side faces, and forms a pair of recirculation bubbles on them (Fig. 9 (c)). But, similarly to flow pattern *I*, there is no reattachment or separation bubble on the counterpart faces of the downstream cylinder and the flow separates from the trailing corners. For instance, this flow pattern is formed in $Re = 100-105$ and $S^* = 4$ ($b_2^* = 4$). Table 6 and Fig. 10 (b, c) provide additional details. The results of pattern *II* show the reattachment points move toward the rear corners of the upstream cylinder and the bubble size is enlarged as Re increases (e.g. see Fig. 10(b, c)).

Flow also separates in pattern *III* from the leading corners of the upstream cylinder but without any reattachment (Fig. 9 (d)). The flow over the downstream cylinder is the same as the two other flow patterns of *I* and *II* ($b_2^* = 4$). The side separation bubbles almost cover the whole side face in flow pattern *III* and due to the collision of the separation bubble on the side surface of the cylinder with the bubble in the gap-spacing, a saddle point (*SD*) emerges adjacent to the rear corners. On the other hand, The *SD* point is a result of the confrontation of the downward motion of the shear layer and the upward motion of the gap flow (Figs. 9 (d), 10 (d)). For example, flow pattern *III* is observed at $Re = 110-150$ ($S^* = 5$, $b_2^* = 4$). Table 6 provides the Re and S^* ranges ($b_2^* = 4$) for the three time-mean flow regimes, where flow pattern *III* is absent at $S^* = 5, 6$.

Besides, Fig. 10 illustrates that a pair of symmetrical recirculation bubbles is formed behind the rectangular cylinder in the mean flow ($b_2^* = 4$ and $S^* = 5$). Based on Fig. 10, the size of this recirculation bubble increases up to $Re = 150$ with increasing Re and then decreases (see Fig. 11).

The previous studies for flow over a single square cylinder reported that flow separation takes place from the rear and front edges of the cylinder at $Re = 100$ and 150 , respectively [9, 14]. Interestingly, this behavior is not similar to that occurs for the upstream cylinder in two tandem cylinders. Based on the mean and instantaneous streamlines consideration in the present work for $S^* = 1-4$ and $Re = 100$ ($b_1^* = 1$, $b_2^* = 4$), the flow separation occurs from the front edge and the separation bubbles form on the side surfaces of the upstream cylinder (flow pattern *II*, see Fig. 9). At $Re = 100$, for $S^* = 5-6$, the flow separates from the rear edge without the formation of separation bubbles on the side surfaces of the upstream cylinder (flow pattern *I*). For $Re > 110$ and $S^* = 5-6$, the flow pattern changes from *I* to *II* (Fig. 9 (a)), where separation occurs from the front edge and the separation bubbles form on the side surfaces of the upstream cylinder (see Fig. 9 for more detail about the position of separation points for various Re and S^*).

Table 5. The parameters of mean flow patterns for various Re ($b_1^* = 1$, $b_2^* = 4$, $S^* = 4$), see also Figs. 9 and 10 (Cyl1: upstream cylinder, Cyl2: downstream cylinder, RC: rear corner, FC: front corner, SP: separation point).

Re	SP (Cyl1)	W_s^* (Cyl1)	L_s^* (Cyl1)	L_d^* (Cyl1)	SP (Cyl2)	Flow pattern
30-95	RC	-	-	-	RC	<i>I</i>
95	RC	-	-	-	RC	<i>I</i>
105	RC & FC	0.03	0.53	0.25	RC	<i>II</i>
110	FC	0.05	0.84	0.20	RC	<i>III</i>
120	FC	0.07	0.55	0.12	RC	<i>III</i>
130	FC	0.09	0.49	0.10	RC	<i>III</i>
140	FC	0.10	0.29	0.07	RC	<i>III</i>
150	FC	0.12	0.11	0.05	RC	<i>III</i>

Table 6. The time-mean flow pattern dependence on the Re and S^* ($b_2^* = 4$).

Pattern	(I)	(II)	(III)
S^*	Re		
1	30-95	100-115	120-150
2	30-95	100-115	120-150
3	30-95	100-105	110-150
4	30-95	100-105	110-150
5	30-110	120-150	-
6	30-115	120-150	-

Figures 10 and 11 provide further insights into the time-mean wake flow. The findings illustrate that the L_r^* and W_r^* change with Re and S^* . Fig. 11(a) shows that $L_r^* = S^*$ for the upstream cylinder when $S^* \leq 4$, regardless of Re , with an exception at $Re = 30$ and $S^* = 4$. On the other hand, shedding the vortices in the gap in the instantaneous sense (e.g. for $S^* = 5, 6$) comes with not filling the gap in the time-mean sense (Fig. 10 (b, c, d)). For $S^* \leq 4$ as the Re increases, the W_r^* for the upstream cylinder increases with a relatively mild slope (Fig. 11 (c)). At $S^* = 5$, the W_r^* increases with Re at first, then suddenly decreases, and afterward varies slightly (Fig. 11 (c)). The variations are similar for W_r^* and L_r^* at $S^* = 5$, as the flow pattern changes from extended-body to co-shedding ($Re = 75-70$). At $S^* = 5$ with gap vortex shedding, the variations of W_r^* and L_r^* with Re are not much (Figs. 11 (a, c)). For the downstream cylinder at $S^* \leq 4$, where the flow is extended-body one, the L_r^* increases up to $Re = 120$ and then decreases (Fig. 10 (b)). The reason for this increase and decrease is related to the base pressure variation of the downstream cylinder. In co-shedding flow for $S^* > 4$, the L_r^* increases with Re (Fig. 11 (b)). The W_r^* for this cylinder mostly increases with Re (Fig. 11 (d)).

The time-mean flow pattern is also understood with the observation of the L_s^* variation (Fig. 10 (d) and Table 5). The separation bubble on the side faces of the upstream cylinder is formed for $S^* = 1-4$ in the range of $100 \leq Re \leq 150$ and for $S^* = 5, 6$ in $Re \geq 120$. In the extended-body flow pattern ($S^* \leq 4$), the L_s^* increases with Re until $Re = 120$ (affiliated to S^*). However, for $Re \geq 120$, it reduces (see e.g. for $S^* = 4$ in Table 5). In the co-shedding flow ($S^* \geq 5$), the L_s^* elongates up to $Re = 150$. The L_s^* in $S^* \geq 5$ with unsteady flow has no variation with increasing S^* and is fixed. Generally, the L_d^* shrinks with increasing Re in both extended-body and co-shedding flows. Besides, the L_d^* is present for mean flow patterns *II* and *III*.

The mean flow patterns were also investigated for a constant gap spacing ($S^* = 4$) and various $b_2^* = 1 - 4$ ($b_1^* = 1$) and $Re = 30-150$. Similar to Figs. 9 and 10, three mean flow patterns *I*, *II*, and *III* were observed for various Re and b_2^* . For example, flow patterns *I* and *II* occur for $Re < 100$ and $Re \geq 100$, respectively, at $b_2^* = 1$. They were *I* and *III* for $Re \leq 100$ and $Re > 100$, respectively, at $b_2^* = 3$. For $b_2^* = 2$, all three mean flow patterns were observed. It should be noted the results for $b_2^* = 4$ are similar to those reported in Figs. 9 and 10 for $S^* = 4$.

4-2-3 Fluctuating stresses

Fluctuating stresses are informative for assimilating the flow behavior. The Reynolds decomposition of velocity gives the time-mean and fluctuating components. Here, similar to

turbulent flows, the fluctuating normal stress components ($\overline{v^*v^*}$ and $\overline{u^*u^*}$), the shear stress $\overline{u^*v^*}$, and the kinetic energy $KE^* = 0.5(\overline{u^*u^*} + \overline{v^*v^*})$ are defined. Figure 12 (a-f) shows the $\overline{u^*u^*}$ and $\overline{v^*v^*}$ contours for $S^* = 1, 4$ and 6 at $Re = 150$. Since those for $S^* = 2, 3$ and $S^* = 5$ respectively give no new insight compared with those of $S^* = 1$ and $S^* = 6$, they have been skipped in this figure. Fig. 12 (g) represents the $(\overline{u^*u^*})_{\max}$ and $(\overline{v^*v^*})_{\max}$ values.

The $\overline{u^*u^*}$ and $\overline{v^*v^*}$ values are close to null in the gap region of cases with $S^* \leq 4$, where the vortices do not shed. They come into being at $S^* > 4$ with the co-shedding flow. The two peaks for $\overline{u^*u^*}$ and one for $\overline{v^*v^*}$ are conspicuous in the wake of the downstream cylinder, regardless of S^* . Accordingly, Fig. 12(g) shows that the $(\overline{u^*u^*})_{\max}$ and $(\overline{v^*v^*})_{\max}$ are relatively small and fixed in the extended-body flow ($S^* \leq 4$) and increase or emerge by turning the flow pattern into co-shedding ($S^* > 4$).

The streamwise distances between the cylinders and the $(\overline{u^*u^*})$ and $(\overline{v^*v^*})$ peaks are denoted as the vortex formation length L_f^* and cross-stream oscillation length L_e^* , see the definitions in Fig. 12 (a, b, e, f) for both cylinders. The L_f^* has an inverse relationship with the mean drag coefficients as well as the RMS of drag and lift for a single cylinder [46, 47]. This inverse relationship is the case between the L_e^* and vortex shedding frequency [14]. More details are provided in sections 4-3-3 and 4-3-4. Fig. 12 (h) portrays the L_f^* and L_e^* variations versus S^* . The L_f^* is present for the upstream cylinder only if $S^* \geq 5$ (i.e. co-shedding flow). But, in the wake of the downstream cylinder, the larger S^* provides the longer L_f^* in the extended-body flow. The trend is reversed when the flow changes to the co-shedding (i.e. $S^* \geq 5$). The L_e^* steadily increases with S^* although it experiences a mild variation at $4 \leq S^* \leq 5$, where the flow pattern changes. The L_e^* and L_f^* for the downstream cylinder are much larger than those for the upstream cylinder in the co-shedding flow (Fig. 12 (h)).

Figure 13 (a-d) displays the shear stress contours $\overline{u^*v^*}$ at $S^* = 1-6$ and $Re = 150$. Since the contours for $S^* = 1 - 4$ are similar, the results for $S^* = 2, 3$ are not displayed for brevity. There are two peaks corresponding to the rolling positions of the two shear layers from two sides of the downstream ($S^*=1-6$) and upstream ($S^*> 4$) cylinders (Fig. 12 (a-d)). As expected in extended-body flow ($S^*= 1-4$), the values of $\overline{u^*v^*}$ are almost zero between two cylinders. In addition, by changing the flow pattern to co-shedding $S^* \geq 5$, the shear stresses of the downstream cylinder are lower than those in extended-body flow ($S^*= 1-4$), (Fig. 13 (a-d, e)).

The streamwise distances between the peaks of $(\overline{u^*v^*})$ and the rear wall of cylinders are defined as L_{uv}^* as seen in 13 (a, b). For the upstream cylinder, the L_{uv}^* is only defined in the co-shedding flow pattern, and a higher S^* leads to a higher L_{uv}^* (Fig. 13 (e)). For the downstream cylinder in the extended-body flow ($S^* \leq 4$), due to the lack of vortex shedding between two cylinders the L_{uv}^* increases with increasing S^* , but in the co-shedding flow pattern ($S^* \geq 5$) it diminishes (Fig. 13 (e)).

The total kinetic energy and the fluctuating stresses on the center line ($y^* = 0$) are shown in the extended-body flow, $S^* = 4$, (Fig. 13 (f)) and co-shedding pattern, $S^* = 6$, (Fig. 13 (g)) at $Re =$

150. In extended-body flow ($S^* \leq 4$), the fluctuating stresses are zero due to the absence of vortex shedding between two cylinders (Fig. 13 (f)). For $S^* \geq 5$ with vortex shedding from both cylinders, the fluctuating stresses and KE^* between cylinders are non-zero and higher than those from the downstream cylinder (Fig. 13 (g)). All the fluctuating stresses for the downstream cylinder in $4 < S_{cr}^* \leq 5$ have an incremental jump due to changing the flow pattern from extended-body to co-shedding flow pattern.

4-3 Global parameters

4-3-1 Local pressure and friction coefficients

Figure 14 (a, b) indicates the time-mean local pressure coefficient (\bar{C}_p) over both cylinders for various S^* ($b_1^* = 1$, $b_2^* = 4$, $Re = 150$). The distributions of \bar{C}_p on the front surface of the upstream cylinder (AB) are similar for all S^* considered (Fig. 14 (a)). In $S^* \leq 4$ (extended-body flow), the absolute values of pressure coefficients in the upper/lower sides and back of the upstream cylinder decrease (or \bar{C}_p becomes less negative) with increasing S^* (Fig. 14 (a)). For $S^* \geq 5$ (the co-shedding flow), the \bar{C}_p on the surfaces (DA-CD-BC) becomes more negative because of the vortex shedding (Fig. 14 (a)). This is also true for the downstream cylinder (Fig. 14 (b)).

A pair of symmetrical recirculation bubbles is formed between two cylinders for $S^* \leq 4$. The \bar{C}_p on the front side of the downstream cylinder (AB) subsequently becomes negative (Fig. 14 (b)). But for the co-shedding flow with $S^* \geq 5$, the pressure on the (AB) is restored and becomes positive (Fig. 14 (b)) as the gap bubbles do not fill the space between the cylinders (Fig. 10 (b, c)). The \bar{C}_p variations on the side faces of the downstream cylinder (BC, DA) depend on S^* . In the extended-body flow pattern ($S^* \leq 4$), the \bar{C}_p values rise from (B) to the middle of the side and then become more negative until the corner (C). Whereas in co-shedding flow $S^* \geq 5$, the \bar{C}_p values increase from (B) to the middle of the side and then it becomes relatively constant to (C) (Fig. 14 (b)).

In Fig. 14 (c, d), the distribution of the mean local friction coefficient \bar{C}_f is shown for both cylinders ($S^* = 1-6$ and $Re = 150$). For the upstream cylinder, the $\bar{C}_f = 0$ at the stagnation point, then grows sharply as it approaches the front corner (B or A). After passing this corner, it decreases sharply because of the flow separation towards the rear corner (C or D) (Fig. 14 (c)). The \bar{C}_f dependence on S^* for the downstream cylinder is different. For $S^* \leq 4$ (EBF), the \bar{C}_f on the front face becomes negative with a zero value at the stagnation point (Fig. 14 (d)). Due to the reattachment point on the side faces ($\bar{C}_f = 0$) at a position of about $0.27b_2^*$ from the front corners, the \bar{C}_f sign changes from negative to positive and then steadily increases (Fig. 14 (d)). But for $S^* \geq 5$ (CSF), the \bar{C}_f becomes positive on the front face (Fig. 14 (d)). Then, it decreases to a relatively constant value in the order of zero along the side faces because of the vortex shedding formation.

4-3-2 Total pressure and frictional drag coefficients

Figure 15 represents the profiles and contours of the time average of total drag (\bar{C}_d), pressure drag (\bar{C}_{dp}), and frictional drag (\bar{C}_{df}) coefficients for various Re and S^* for both cylinders ($b_1^* = 1$, $b_2^* = 4$). The line with the circle in Fig. 15 (c, d) shows the Re_{cr} , and the dashed lines divide the time-mean flow patterns. Fig. 15 (a) shows that the \bar{C}_d of both cylinders at $S^* \leq 4$ steadily decreases with increasing Re . For both cylinders at $S^* = 5$, a jump is observed in \bar{C}_d (Fig. 14 (a, b)) at $Re = 70-75$ where the vortex shedding occurs, and flow pattern changes from steady extended-body to co-shedding (see also Fig. 8 (a)). Fig. 15 (a-d) demonstrates that the \bar{C}_d values of both cylinders in the co-shedding flow pattern ($S^* \geq 5$) are larger than those in the extended-body flow pattern ($S^* \leq 4$). In the *EBF* pattern for the downstream cylinder ($b_2^* = 4$), the symmetrical vortices in the gap cause a strong suction on the front face of the downstream cylinder. The negative pressure on this face makes the drag force of this cylinder negative for $S^* \leq 4$ but it depends on Re , e.g. at $S^* = 1$ for $Re > 100$ (Fig. 15 (b, d)).

Since $\bar{C}_d = \bar{C}_{dp} + \bar{C}_{df}$, scrutiny of \bar{C}_{dp} and \bar{C}_{df} comes with further drag variation clarification. The \bar{C}_{dp} behavior is almost similar to \bar{C}_d for both cylinders (Fig. 15 (e, f)) because the \bar{C}_{df} is generally smaller than \bar{C}_{dp} , although \bar{C}_{df} at low Reynolds numbers (dependent on Re and S^*) has a noticeable contribution [20]. The \bar{C}_{df} decreases with Re for both cylinders (Fig. 15 (g, h)). By increasing Re , the separation points of the upstream cylinder shift from rear corners to front ones, and the recirculation bubbles are formed on its side faces. This makes \bar{C}_{df} negative for $S^* \leq 4$ at $Re = 150$ (e.g., see Fig. 14 (c), Fig. 15 (g)). For the downstream cylinder, there is neither the separation bubble nor the flow reattachment. Therefore, the \bar{C}_{df} remains positive (e.g., Fig. 15 (h)).

4-3-3 RMS lift and drag coefficients

How the C_{lrms} and C_{drms} are dependent on Re and S^* is illustrated in Fig. 16 ($b_1^* = 1$, $b_2^* = 4$). These two coefficients show the force fluctuation level caused by vortex shedding and mainly increase with increasing Re . They are zero in the steady flow, e.g. $Re < 100$ for $S^* \leq 4$ ($b_1^* = 1$, $b_2^* = 4$), see Fig. 8 and 16. In the extended-body flow pattern for $S^* \leq 4$, the C_{lrms} for the upstream cylinder is in order of zero, while for the downstream cylinder is not zero but it is not much (Fig. 16 (a, b)). At $Re > 120$, it increases slightly. However, the C_{lrms} increases with increasing Re for both cylinders in a co-shedding flow pattern, e.g. at $S^* = 6$. This increase is more significant for the downstream cylinder (Fig. 16 (a, b)).

The C_{drms} is zero in extended-body flow ($S^* \leq 4$) for the upstream cylinder. Fig.16 (c) shows the C_{drms} raises as the strength of vortices increases at higher Re for both cylinders. The impinging gap vortices produce a lower fluctuation force on the upstream cylinder compared to the downstream cylinder. Hence, C_{drms} is higher on the downstream cylinder (Fig. 16 (c)). For $S^* \geq 5$ with vortex shedding and increasing S^* ($Re \leq 100$), the C_{drms} grows for the downstream cylinder, while its variation is insignificant for $Re > 100$.

As mentioned, the L_f^* has an inverse relationship with the RMS of drag and lift for a single cylinder [46, 47]. While, for two tandem cylinders, it depends on the S^* and flow pattern. A higher L_f^* and S^* corresponded to lower C_{lrms} for the upstream cylinder in the co-shedding flow. But, the L_f^* has a direct relationship with C_{lrms} and S^* for the downstream cylinder in extended-body flow (Fig. 12 (a-d, h) and Fig. 16 (a, b)).

4-3-4 Vortex shedding frequency

Figure 17 illustrates the Strouhal number (St) as a function of Re and S^* ($b_1^* = 1, b_2^* = 4$). The contour incorporates the Re_{cr} and the time-mean flow pattern boundaries. The St is determined from the fast Fourier transform (FFT) of the fluctuating lift. As expected, the $St = 0$ for cases with $Re < Re_{cr}$ and the upstream cylinder in the extended-body flow pattern ($S^* \leq 4$). For $S^* \leq 4$, the St associated with the downstream cylinder increases with increasing Re and decreases insignificantly with S^* . Nonetheless, the St is the same for both cylinders and increases with increasing Re and S^* for $S^* \geq 5$ (i.e., co-shedding flow pattern), which can be ascribed to elongated L_e^* with S^* . For the single cylinders, the L_e^* has an inverse relationship with St [14, 43]. A comparison of Figs. 12 (h) and 17 (a) reveal that the L_e^* and St variations with S^* similarly have opposite trends when $S^* \leq 4$ (i.e. extended-body flow pattern). But, for the co-shedding flow pattern, the L_e^* and St both increase with S^* . Equations (8) and (9) reflect our simulation results for the vortex shedding frequency, showing how St varies with Re and S^* ($b_1^* = 1, b_2^* = 4$). These equations respectively deviate $\sim 4.5\%$ and 3% from data in Fig. 17 at the most.

$$St = \left(0.05 + \frac{0.001}{S^* + 0.07}\right) \ln(Re) - 0.1263, \quad S^* \leq 4, \quad \text{For Cyl 2}, \quad (8)$$

$$St = \left(\frac{0.5}{S^*} + 1.9\right) \times 10^{-6} Re^2 + \left(\frac{0.00075 S^*}{S^* + 0.05}\right) Re + 0.081, \quad S^* \geq 5, \quad \text{For Cyl 1, 2}, \quad (9)$$

4-4 Hysteresis phenomena

The dependence of flow characteristics on the approaching manner of Re and/or S^* into the target flow condition (i.e. the flow history) is called hysteresis in the context of flow over cylinders in arrangements. In other words, hysteresis is a phenomenon of the flow resisting changing the flow pattern. It is mainly observed in a range around the Re or S^* thresholds, in which the flow pattern transits. It is numerically investigated by applying different initial conditions, where two different aerodynamic responses are observed in a given S^* and Re [19, 20, 23, 25]. The experimental studies gradually increase and decrease the S^* , for a given Re [22, 24]. The S^* and/or Re range, in which this phenomenon is observed, is known as the hysteresis limit.

The hysteresis here is studied in various $S^* = 1-6$ at $Re = 150$ ($b_1^* = 1, b_2^* = 4$). Three different initial conditions are applied for a given S^* to find the hysteresis limit and are named A, B, and C conditions. In case A, the simulation is started with a fluid at rest. In case B, an already simulated case for a larger S^* (e.g. the flow field for a case with $S^* = 5$ is mapped into and initialized the case with $S^* = 4$) serves as the initial condition, while Re is fixed for both of them. The procedure

is reversed in case C, compared with case B, i.e., the data of a smaller S^* initializes the case with a larger S^* . The hysteresis in this study is observed at $3.5 \leq S^* \leq 4.5$. Two distinct responses in the hysteresis limit are seen (Fig. 18) and referred to here as mode 1 (extended-body flow pattern or *EBF*) and mode 2 (co-shedding flow pattern or *CSF*), i.e., cases A and C come with the same results.

Figure 19 shows the variations of total drag coefficient (\bar{C}_d), RMS lift coefficient (C_{lrms}), and Strouhal number (St), in which the hysteresis limit (*HL*) has been marked. In *HL*, the two branches correspond to Mode 1 and Mode 2. In other words, the flow pattern is either the extended-body flow (Mode 1 or *EBF*) or co-shedding flow (Mode 2 or *CSF*) outside the *HL* region, regardless of the initial condition. However, the initial condition ascertains which flow pattern to emerge in the *HL*.

The \bar{C}_d gradually decreases for the upstream cylinder and moderately increases for the downstream cylinder with increasing S^* for Mode 1. An abrupt increase is then observed in the \bar{C}_d of both cylinders in the *HL* due to shifting flow mode (Fig. 19 (a, b)). The drag coefficients associated with Mode 1 are smaller than those of Mode 2 in the *HL* (Fig. 19 (a, b)). The \bar{C}_d of both cylinders gradually increases with S^* in Mode 2 (*CSF*). It is worth noting that the \bar{C}_d values for a given S^* are larger for the upstream cylinder in both modes (Fig.18 (a-b)). RMS lift coefficients (C_{lrms}) are illustrated in Fig. 19 (c, d) for both modes and cylinders. The C_{lrms} values for both cylinders are remarkably larger in Mode 2 (Fig. 19 (c, d)), where vortex shedding occurs from both cylinders (*CSF*). Similarly, the St is noticeable where the vortex shedding occurs (Fig. 19 (e)). However, the trend is a bit different from C_{lrms} .

Although the hysteresis for the tandem cylinders with square and rectangular cross-sections is reported for the first time in the literature, a comparison of results with similar studies over two tandem square cylinders is worthy. The *HL* range was reported as $2.5 \leq S^* \leq 4.75$ for two tandem square cylinders at $Re = 150$ [20, 23, 26]. Consequently, an increase in the downstream cylinder aspect ratio results in an *HL* decrement.

4-5 Discussion

The influence of Re , b_2^* , and S^* on the flow features was investigated in the previous sections. We here aim to take a closer look into the results to relate the flow behavior and its correlation with the engineering parameters. Figure 20 represents the correlation of the time-mean flow pattern (*MFP*; *I*, *II*, *III*) and instantaneous flow pattern (*IFP*; i.e., extend-body flow or *EBF* and co-shedding flow or *CSF*) discussed in previous sections. Table 7 (a, b), on the other hand, renders qualitative variations of global characteristics, fluctuating stress, and kinetic energy in different flow patterns ($b_1^* = 1$, $b_2^* = 4$, $S^* = 1 - 6$, $Re = 30-150$).

To compare the flow physics and correlate the aerodynamic characteristics and flow patterns, two Reynolds numbers of 70 and 150 associated with the steady and unsteady flows (i.e. before and after the onset of vortex shedding), are considered. At $Re = 70$ and $1 \leq S^* \leq 4$, the time-mean flow is *I* (steady) and the flow separation takes place from the trailing edge of the upstream cylinder, similar to that occurs from a square cylinder up to $Re = 100$ [9]. The flow is then

attached to the side surfaces of the downstream cylinder and separated again from the downstream cylinder trailing corners. The time-mean flow I at $Re = 70$ corresponds to the steady flow for $S^* \leq 5$ and unsteady flow for $S^* = 6$ (co-shedding flow pattern), see Figs. 8, 9 and 20 (a, b). Thus, an increase of S^* changes the steady flow to co-shedding flow although the separation still takes place from the rear edge of the cylinders (Fig. 20 (b)).

At $S^* = 1-3$ and $Re = 150$, the time-average streamlines are separated from the front edges of the upstream cylinder and stick to the side surfaces of the downstream cylinder (Fig. 20 (c)). The *EBF* and *III* flow patterns are found from instantaneous and mean flows, respectively, see Figs. 8 and 9. Due to the hysteresis phenomena both *EBF* and *CSF* were observed at $S^* = 4$, $Re = 150$. These two instantaneous flow patterns are observed in Fig. 20 (d) and are denoted as Mode 1 and Mode 2, respectively. The corresponding mean-flow patterns are *II* and *III*, respectively (Figs. 9, 10, and 20 (c)). At $S^* = 6$ and $Re = 150$, the instantaneous and mean flow patterns are *CSF* and *II*, respectively, see Fig. 20 (e).

To obtain a qualitative relationship between the aerodynamic characteristics and flow patterns; two cases are considered. First at a constant $Re = 150$, S^* varies from 1-6 (Table 7 (a)). Second, Re changes from 30 to 150 at a constant $S^* = 6$ (Table 7 (b)).

Table 7 (a) indicates that the vortex shedding frequency, force fluctuations, shear stress, and kinetic energy for the upstream cylinder are null, while the length and width of the vortices behind the upstream cylinder (L_r^* , W_r^*) increase and consequently, the \bar{C}_{dp} and \bar{C}_d decrease (also see Figs. 11 and 15) when S^* changes from 1 to 4 at $Re = 150$ (*EBF*, mean flow patterns *II* and *III*). For the downstream cylinder by changing S^* from 1 to 4, the drag coefficient and force fluctuations increase, while the other parameters in Table 7 (a) decrease (*CSF*, mean flow patterns *II* and *III*). For $S^* = 5, 6$, the co-shedding flow pattern occurs and variations of parameters are not similar to those for $S^* = 1-4$ (Table 7 (a)). For example, the KE^* , L_r^* , and St increase for the upstream cylinder, while the $\overline{u^*v^*}$ and RMS lift and drag decrease. For the downstream cylinder, the L_r^* decreases, while \bar{C}_d , C_{drms} , St , W_r^* , and KE^* increase.

In the second case, because the cylinder gap-spacing is considered constant ($S^* = 6$) and the Reynolds number increases ($Re = 30-150$), both steady ($Re < Re_{cr}$) and unsteady ($Re > Re_{cr}$) flow behavior appears (Table 7 (b)). Thus, at $S^* = 6$, with increasing $Re = 30-150$ and mean flow patterns *I*, *II*, unsteady *MFP*, and *CSF*, an increment was observed in the RMS lift and drag, vortex shedding frequency, fluctuating stress, and kinetic energy for both cylinders. The L_r^* variation has different behavior and decreases in *EBF* for the upstream cylinder and increases for the downstream cylinder, and it is related to the base pressure of the cylinders. Only W_r^* remains unchanged for the upstream cylinder in the *CSF* (Table. 7 (b)). The \bar{C}_d reduces for both cylinders in any case (Fig. 15 and Table 7 (b)).

Table 7. Qualitative variations of engineering parameters, fluctuating stress, and kinetic energy in different flow patterns for various S^* and Re ($b_1^* = 1, b_2^* = 4$), (a): $S^* = 1 - 6, Re = 150$, (b): $S^* = 6, Re = 30-150$.

IFP	Cyl	MFP	\bar{C}_d	Increase		St	Unchanged	Decrease		KE^*
				C_{lrms}	C_{drms}		L_r^*	W_r^*	$\bar{u}^* \bar{v}^*$	
(a) $S^* = 1-6$ $Re = 150$										
EBF, $S^* = 1-4$	1	<i>II, III</i>	Red	0	0	0	Green	Green	0	0
	2	<i>II, III</i>	Green	Green	Green	Red	Red	Red	Red	Red
CSF, $S^* = 5, 6$	1	<i>II, III</i>	Yellow	Red	Red	Green	Green	Yellow	Red	Green
	2	<i>II, III</i>	Green	Green	Yellow	Green	Red	Green	Yellow	Green
(b) $S^* = 6$ $Re = 30-150$										
EBF, $Re < Re_{cr}$	1	<i>I, II</i>	Red	Green	Green	Green	Red	Green	Green	Green
	2	<i>I, II</i>	Red	Green	Green	Green	Green	Green	Green	Green
CSF, $Re > Re_{cr}$	1	<i>I, II</i>	Red	Green	Green	Green	Red	Yellow	Green	Green
	2	<i>I, II</i>	Red	Green	Green	Green	Green	Green	Green	Green

5- Conclusions

The results of flow around tandem Sharp-edged cylinders of diverse cross sections at different cylinder gap-spacing $S^* = 1-6$ and $Re = 30-150$ were investigated. The aspect ratio of the downstream rectangle cylinder ($b_2^* = 1 - 4$) was also studied. The ranges of critical Reynolds number (Re_{cr}) that vortex shedding occurs and the flow changes from steady to unsteady were determined for both cylinders for various b_2^* and S^* . Besides, the instantaneous (extended-body flow (EBF) and co-shedding flow (CSF)) and time-mean flow (*I, II, III*) structure along with the details of the flow (aerodynamic parameters and fluctuating stresses) around the cylinders were analyzed.

The Re_{cr} changes for two tandem square $b_1^* = 1$ and rectangular $b_2^* = 4$ cylinders as a second and third-order polynomial (Eqs. 6 and 7), the Re_{cr} decreases from 128 ± 2 to 50 ± 2 with S^* increasing from 1 to 6. A smaller Re is thus required for a larger S^* to have the onset of vortex shedding ($b_1^* = 1, b_2^* = 4$). However, at $S^* = 4$ for two tandem square cylinders ($b_1^* = b_2^* = 1$), $Re_{cr} = 78 \pm 2$ is the same for both cylinders, but $Re_{cr} = 165 \pm 2, 145 \pm 2$ and 93 ± 2 for $b_2^* = 2, 3$ and 4, respectively. So, at a fixed $S^* = 4$, with the aspect ratio's growth of the downstream cylinder $b_2^* = 1-4$, the Re_{cr} for the downstream cylinder first increases up to $b_2^* = 2$ and then decreases. The elongated streamwise length of the downstream cylinder stabilizes the flow like a splitter plate. In $S^* = 4$ by increasing the downstream cylinder aspect ratios, the vortex shedding is present for

both cylinders at $b_2^* = 1$ (*CSF*), suppressed for both cylinders up to $Re_{cr} = 165 \pm 2$ ($b_2^* = 2$) and then stopped for the upstream cylinder at $b_2^* = 3, 4$ for $Re_{cr} < Re \leq 150$ (*EBF*).

Two instantaneous flow patterns are apperceived and in the ranges of Re , S^* and b^* examined. In extended-body flow (*EBF*), the shear layers separated from the upstream cylinder stick to the surface of the downstream cylinder, and vortex shedding just occurs from the downstream cylinder. This flow pattern has been observed at $S^* \leq 4$, and $Re = Re_{cr} - 150$ for two tandem cylinders ($b_1^* = 1$, $b_2^* > 2$). In the co-shedding flow (*CSF*), the vortex shedding takes place simultaneously between two cylinders and behind the downstream cylinder. This flow pattern can be seen in $Re = Re_{cr} - 150$ at $S^* \geq 5$ ($b_1^* = 1$, $b_2^* = 1, 4$). For $b_1^* = 1$, $b_2^* = 2$, flow over both cylinders becomes steady up to $Re = Re_{cr} = 165 \pm 2$.

Three distinct flow patterns (*I*, *II*, and *III*) of mean flow are identified. In pattern *I* (rear-corner separated flow) the flow is completely parallel to the upper and lower surfaces of the upstream cylinder and no reattachment or separation bubble is created on the cylinder surfaces. In pattern *II* (separation bubble flow), flow separates from the front side of the upstream cylinder and a pair of separation bubbles is formed on the upper and lower surfaces of the upstream cylinder and then, the reattachment point is created on those surfaces. In pattern *III* (front-corner separated flow) the separation bubble on the upper and lower surfaces covers almost the entire surface of the upstream cylinder and no reattachment point is observed. A saddle point emerges above the upstream cylinder rear corners. For $b_1^* = 1$, $b_2^* = 4$, mean flow pattern *I*, prevails at $S^* \leq 4$ in $Re = 30-95$, pattern *II* appears at $S^* \geq 5$ in $Re = 120-150$ and pattern *III* emerges at $S^* \leq 2$ in $Re = 120-150$. Pattern *III* has not been observed for $S^* = 5, 6$, while it occurs for $S^* \leq 4$ and $Re > 105$.

Fluctuation stresses perpendicular to the flow (normal stress) are stronger than those in the flow direction and are more noticeable in unsteady flow between two cylinders. In both mean flow patterns (*II* and *III*), the $(\overline{v^* \overline{v^*}})$ is the maximum oscillating stress, which contributes more to the total kinetic energy. All the fluctuating stresses for the downstream cylinder in $4 < S_{cr}^* \leq 5$ and the range of changing flow from quasi-steady to unsteady have an incremental jump.

Aerodynamic parameters are completely influenced by Re , S^* , downstream cylinder aspect ratios (b_2^*), and flow patterns when the Re increases and the instantaneous flow pattern changes from extended-body (*EBF*) to co-shedding (*CSF*), an increase in all aerodynamic parameters was observed for the two cylinders. Aerodynamic parameters, except base pressure behind the cylinders, after variation in the flow pattern and incremental jump, continue their previous behavior with the increase of Reynolds number. Recirculation bubbles size behind the cylinders as well as the length of the vortex formation have an inverse relationship with base pressure behind both cylinders.

The results of this research authenticate the hysteresis limit for flow around two tandem cylinders ($b_1^* = 1$, $b_2^* = 4$) occurs in cylinder gap-spacing $3.5 \leq S^* \leq 4.5$ ($Re = 150$). In the hysteresis limit, two branches are observed. Each branch corresponds to an instantaneous flow pattern. The lower branch indicates extended-body flow where there is no vortex shedding between two cylinders (Mode 1). While the upper branch represents a co-shedding flow pattern (Mode 2). Hence, the hysteresis limit depends on the Reynolds number, cylinder gap spacing,

and aspect ratio of the upstream cylinder. It is noteworthy that in all situations and for both cylinders, the drag coefficient, $C_{l_{rms}}$, and Strouhal number in Mode 2 are higher than those of Mode 1.

Reference

1. J. Mizushima and N. Suehiro. "Instability and transition of flow past two tandem circular cylinders". *Phys. Fluids*, 17(10): 104107 (2005).
2. A. Sohankar, S. Mohagheghian, A. A. Dehghan, and M. D. Manshadi. "A smoke visualization study of the flow over a square cylinder at incidence and tandem square cylinders". *J vis*, 18: p. 687-703 (2015).
3. J. Aboueian, and A. Sohankar. "Identification of flow regimes around two staggered square cylinders by a numerical study". *Theor. Comput. Fluid Dyn*, 31: p. 295-315 (2017).
4. L. J. Wang, M. M. Alam, and Y. Zhou. "Two tandem cylinders of different diameters in cross-flow: Effect of an upstream cylinder on wake dynamics". *J. Fluid Mech*, 836: 5–42 (2018).
5. A. Sohankar, M. Abbasi, M. Nill-Ahmadabadi, M. Alam and F. Zafar, "Experimental study of the flow around two finite square cylinders". *Archives of Mechanics* 70, 457–480 (2018).
6. F. Freidooni, A. Sohankar, M. R. Rastan, and E. Shirani. "Flow field around two tandem non-identical-height square buildings via LES". *Build. Environ.* 201: 107985 (2021).
7. J. Aboueian, A. Sohankar, M. R. Rastan, M. Ghodrat. "An experimental study on flow over two finite wall-mounted square cylinders in a staggered arrangement". *Ocean Eng*, 240: 109954, (2021).
8. M. M. Alam, M. R. Rastan, L. Wang, and Y. Zhou. "Flows around two nonparallel tandem circular cylinders". *J. Wind Eng. Ind. Aerodyn*, 220: 104870 (2022).
9. A. Sohankar, C. Norberg, and L. Davidson. "Low-Reynolds-number flow around a square cylinder at incidence: study of blockage, onset of vortex shedding and outlet boundary condition". *Int. J. Numer. Methods Fluids*, 26: p. 39–56 (1998).
10. A. Sohankar, C. Norberg, and L. Davidson. "Simulation of three-dimensional flow around a square cylinder at moderate Reynolds numbers". *Phys. Fluids*, 11: p. 288-306 (1999).
11. H. Jiang, and L. Cheng. "Flow separation around a square cylinder at low to moderate Reynolds numbers". *Phys. Fluids*, 32(4): 044103 (2020).
12. H. Jiang and L. Cheng. "Transition to chaos in the cylinder wake through the Mode C flow". *Phys. Fluids*, 32: 014103 (2020).
13. M. R. Rastan, H. Shahbazi, A. Sohankar, M. M. Alam, and Y. Zhou. "The wake of a wall-mounted rectangular cylinder: Cross-sectional aspect ratio effect". *J. Wind Eng. Ind. Aerodyn*, 213: 104615 (2021).
14. A. Mashhadi, A. Sohankar, and M. M. Alam. "Flow over rectangular cylinder: Effects of cylinder aspect ratio and Reynolds number". *Int. J. Mech. Sci*, 195: 106264 (2021).
15. M. R. Rastan, M. M. Alam, H. Zhu, and C. Ji. "Onset of vortex shedding from a bluff body modified from square cylinder to normal flat plate". *Ocean Eng*, 244: 110393, (2022).
16. A. Mashhadi, and A. Sohankar, "Two- and three-dimensional simulations of flow and heat transfer around rectangular cylinders". *Comput. Fluids*, 249, 105689 (2022).

17. T. Liu, L. Zhou, D. Huang, H. Zhang, and C., Wei. "Aspect ratio and interference effects on flow over two rectangular cylinders in tandem arrangement". *Ocean Eng*, 271: p. 113731 (2023).
18. A. Sohankar, and A. Etminan. "Forced-convection heat transfer from tandem square cylinders in cross flow at low Reynolds numbers". *Int. J. Numer. Methods Fluids*, 60: p. 733–751 (2009).
19. M. R. Rastan, and M. M. Alam. "Transition of wake flows past two circular or square cylinders in tandem". *Phys. Fluids*, 33: 081705 (2021).
20. A. Sohankar. "A numerical investigation of the flow over a pair of identical square cylinders in a tandem arrangement". *Int. J. Numer. Methods Fluids*, 70: p. 1244–1257 (2012).
21. B. S. Carmo, J. R. Meneghini, and S. J. Sherwin. "Possible states in the flow around two circular cylinders in tandem with separations in the vicinity of the drag inversion spacing". *Phys. Fluids*, 22: 054101 (2010).
22. C. H. Liu, and J. M. Chen. "Observations of hysteresis in flow around two square cylinders in a tandem arrangement". *J. Wind Eng. Ind. Aerodyn*, 90: p. 1019-1050 (2002).
23. A. Sohankar, E. Rangraz, M. Khodadadi, and M. D. Mahbub Alam. "Fluid flow and heat transfer around single and tandem square cylinders subjected to shear flow". *J. Braz. Soc. Mech. Sci. Eng*, 42: 414 (2020).
24. J. Sobczyk, W. Wodziak, R. Gnatowska, J. Stempka, and P. Niegodajew. "Impact of the downstream cylinder displacement speed on the hysteresis limits in a flow around two rectangular objects in tandem-PIV study of the process". *J. Wind Eng. Ind. Aerodyn*, 179: 184–189 (2018).
25. A. Sohankar. "A LES study of the flow interference between tandem square cylinder pairs". *Theor Comput. Fluid Dyn*, 28: p. 531-548 (2014).
26. F. Nikfarjam, and A. Sohankar. "Study of hysteresis associated with power-law fluids past square prisms arranged in tandem". *Ocean Eng*, 104: p. 698-713 9 (2015).
27. M. K. Kim, D. K. Kim, S. H. Yoon, and D. H. Lee. "Measurements of the flow fields around two square cylinders in a tandem arrangement". *J. Mech. Sci. Technol*, 22: 397 (2008).
28. S .C. Yen, K .C. San, and T. H. chuang. "Interactions of tandem square cylinders at low Reynolds numbers". *Exp. Therm. Fluid Sci*, 32(4): p. 927-938 (2008).
29. F. Nikfarjam, and A. Sohankar. "Power-law fluids flow and heat transfer over two tandem square cylinders: effects of Reynolds number and power-law index". *Acta Mech*, 224: p. 1115-1132 (2013).
30. D. Xiaiqing, X. Hanlin, M. Wenyong, D. chin, and L. Qingkuan. "Experimental study on aerodynamic characteristics of two square cylinders at various incidence angles". *J. Wind Eng. Ind. Aerodyn*, 191: p. 154-169 (2019).
31. J. Y. Shao, C. Shu, N.Y. Liu, and X. Zhao. "Numerical investigation of vortex-induced rotation of two square cylinders in tandem arrangement". *Ocean Eng*, 171: 485–495 (2019).
32. D. Kumar, K. Sourav, and S. Sen. "Steady separated flow around a pair of identical square cylinders in tandem array at low Reynolds numbers". *Comput. Fluids*, 191. 104244 (2019).

33. J. Shang, Q. Zhou, M. M. Mahbub Alam, H. Liao, and S. H. Cao. “Numerical studies of the flow structure and aerodynamic forces on two tandem square cylinders with different chamfered-corner ratios”. *Phys. Fluids*, 31, 075102 (2019).
34. Q. Shui, C. Duan, D. Wang and Z. H. Gu. “New insights into numerical simulations of flow around two tandem square cylinders”. *AIP Adv.* 11: 1-14 (2021).
35. Z. ul-Islam, S. ul-Islam, and C. Y. Zhou. “The wake and force statistics of flow past tandem rectangles”. *Ocean Eng.* 236: p. 109476 (2021).
36. C. Zhang, X. Wang, L. Song, and L. Ran. “Temperature Hysteresis Mechanism and Compensation of Quartz Flexible Accelerometer in Aerial Inertial Navigation System”. *Sensors*, 21: 10.3390 (2021).
37. J. Rabault, M. Kuchta, A. Jensen, U. R. Eglade, and N. Cerardi. “Artificial neural networks trained through deep reinforcement learning discover control strategies for active flow control”. *J. Fluid Mech.* 865: 281–302 (2019).
38. A. Sohankar, M. Khodadadi, E. Rangraz, and M. D. Mahbub Alam. “Control of flow and heat transfer over two inline square cylinders”. *Phys. Fluids*, 31: 123604 (2019).
39. M. R. Rastan, A. Sohankar, and M. M. Alam. “Flow and heat transfer across two inline rotating cylinders: Effects of blockage, gap spacing, Reynolds number, and rotation direction”. *Int. J. Heat Mass Transfer*, 174: 121324 (2021).
40. A. Sharma, and V. Eswaran. “Heat and fluid flow across a square cylinder in the two-dimensional laminar flow regime”. *Numer. Heat Transf. Part A Appl.* 45(3): 247–69 (2004).
41. S. Sen, S. Mittal, G. Biswas, T. Muramatsu, and G. Yagawa. “Flow past a square cylinder at low Reynolds numbers”. *Int. J. Numer. Methods Fluids.* 67: 1160–74 (2011).
42. Q. Zheng, and M. Alam. “Intrinsic features of flow past three square prisms in side-by-side arrangement”. *J. Fluid Mech.* 826: 996–1033 (2017).
43. M. M. Alam, T. Abdelhamid, and A. Sohankar. “Effect of cylinder corner radius and attack angle on heat transfer and flow topology”. *Int. J. Mech Sci.* 175: 105566 (2020).
44. J. C. R. Hunt, A. A. Wray, and P. Moin. “Eddies, stream, and convergence zones in turbulent flows”. *Cent. Turbul. Res. Rep. CTR-S88*, pp. 193–208 (1988)
45. J. Jeong, and F. Hussain. “On the identification of a vortex” *J. Fluid Mech.* 285, 69–94 (1995)
46. M. S. Bloor. “The transition to turbulence in the wake of a circular cylinder”. *J. Fluid Mech.* 19: 290-304 (1964).
47. M. M. Alam, Y. Zhou. “Turbulent wake of an inclined cylinder with water running”. *J. Fluid Mech.* 589, 261-303 (2007).

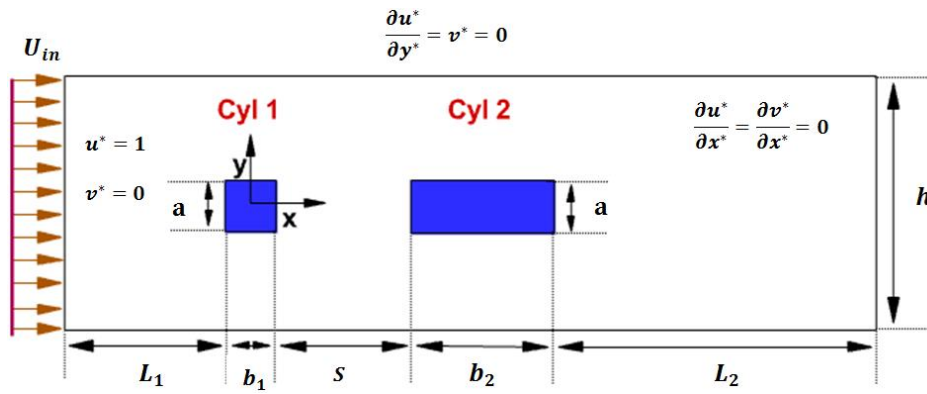


Figure 1. Computational domain and boundary conditions for the problem under consideration (Cyl1: upstream cylinder; Cyl2: downstream cylinder).

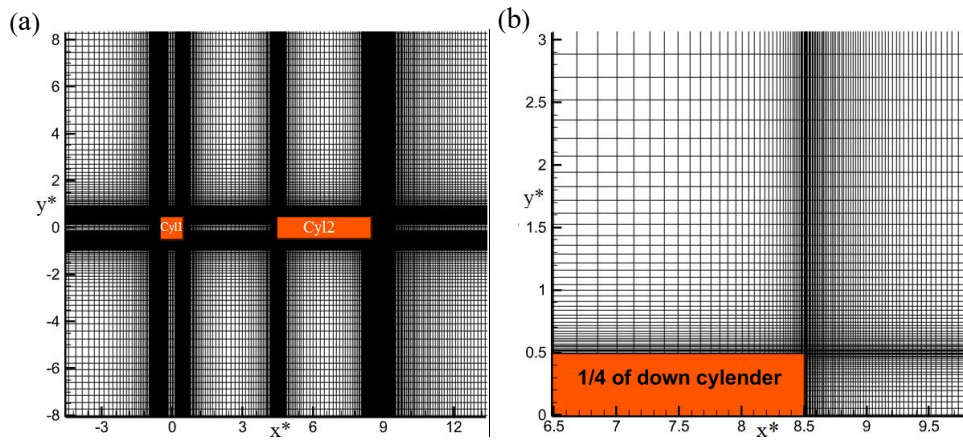


Figure 2. The close-up grid ($b_1^* = 1$, $b_2^* = 4$, $S^* = 4$) in (a) around two cylinders and (b) around 1/4 downstream cylinder.

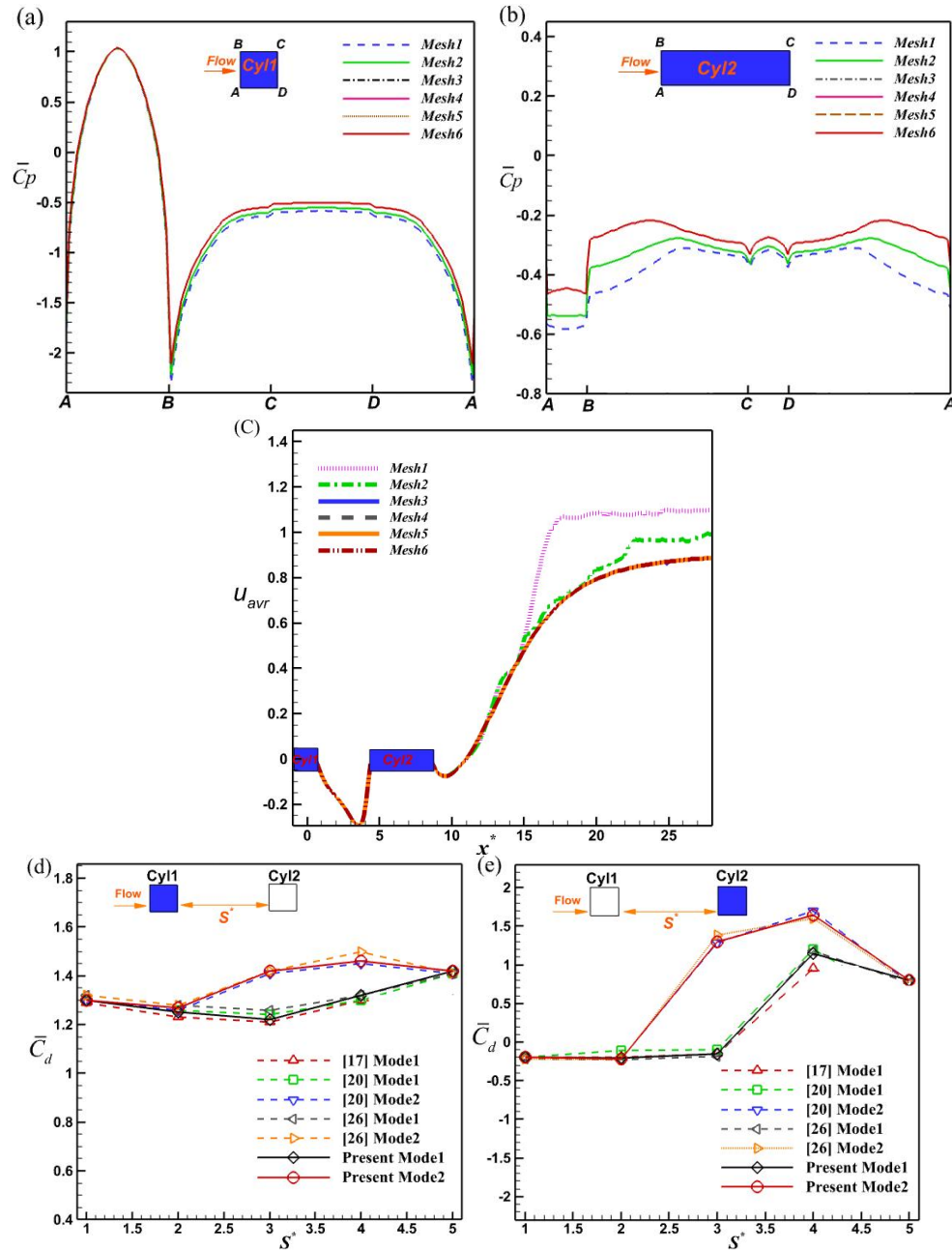


Figure 3. Grid study and validation test ($Re = 150$). The local pressure coefficient on the cylinders surfaces (a) Cyl1 ($b_1^* = 1$), (b) Cyl2 ($b_2^* = 4$), (c) the mean velocity on the centerline ($y=0$) for various grids ($S^* = 4$). \bar{C}_d comparison with [17, 20, 26] as a validation test for two tandem square cylinders at different S^* (d) Cyl1 ($b_1^* = 1$), (e) Cyl2 ($b_2^* = 1$).

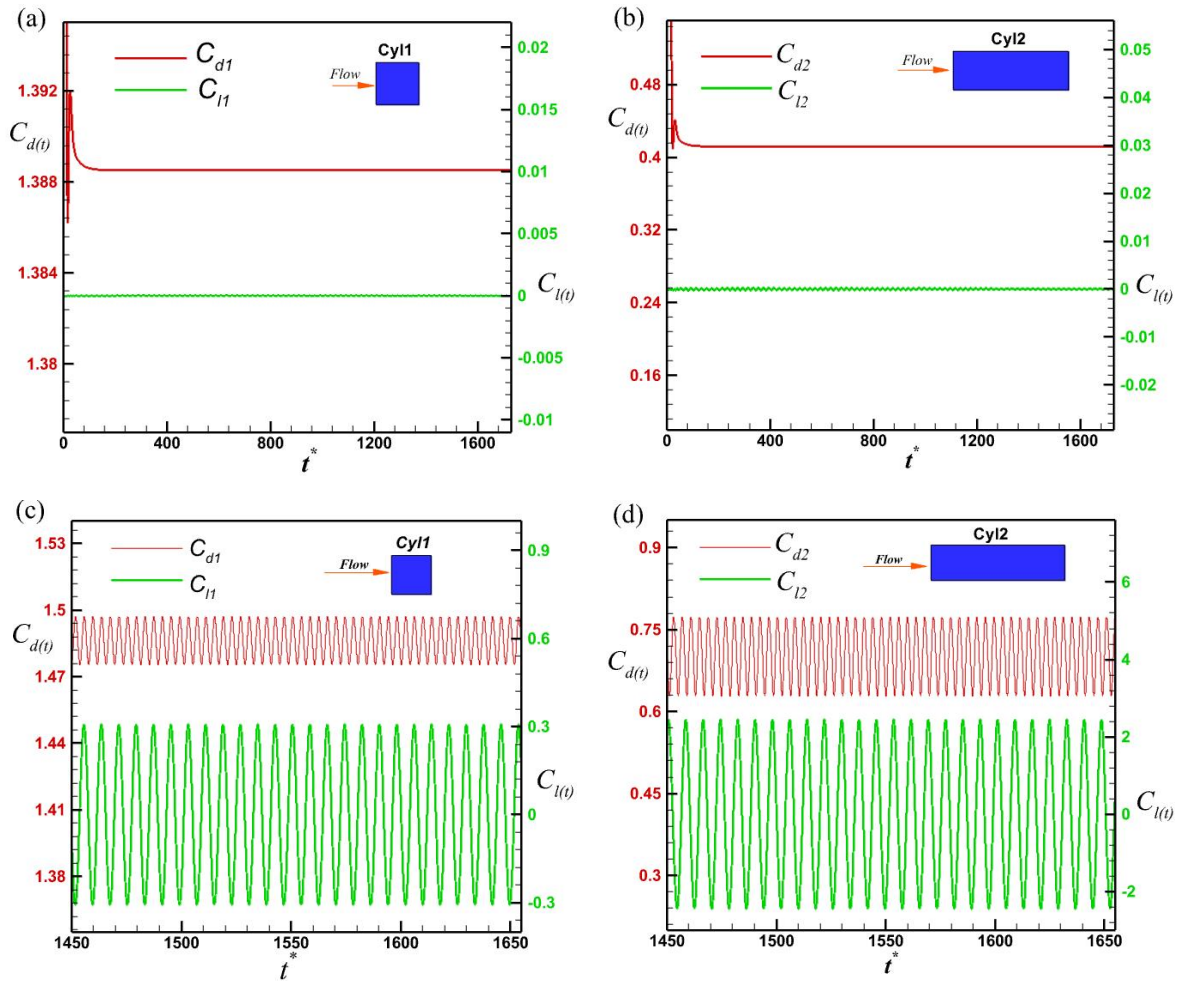


Figure 4. The lift and drag coefficient signals of both cylinders for (a, b) steady ($S^* = 5$ and $Re = 70$) and (c, d) unsteady flows ($S^* = 4$ and $Re = 75$).

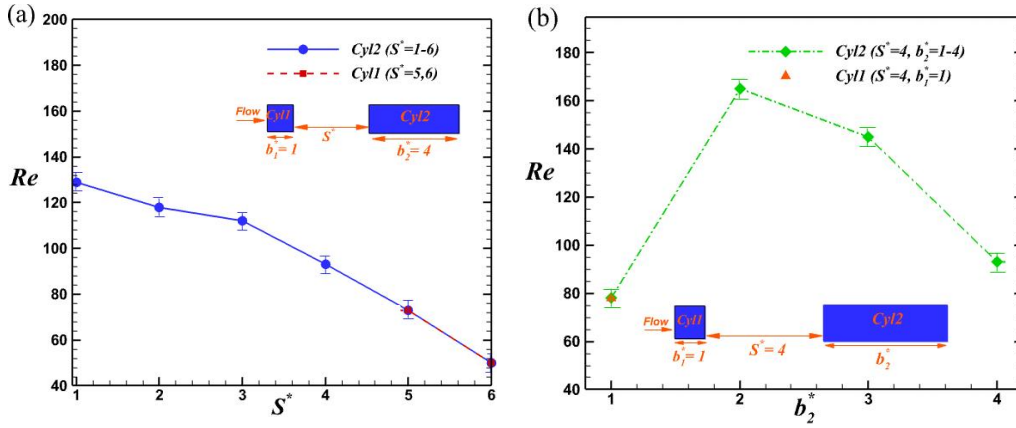


Figure 5. The variation of critical Reynolds numbers (Re_{cr}) for various (a) $S^* = 1 - 6$ ($b_1^* = 1$, $b_2^* = 4$) and (b) $b_2^* = 1 - 4$ ($S^* = 4$, $b_1^* = 1$).

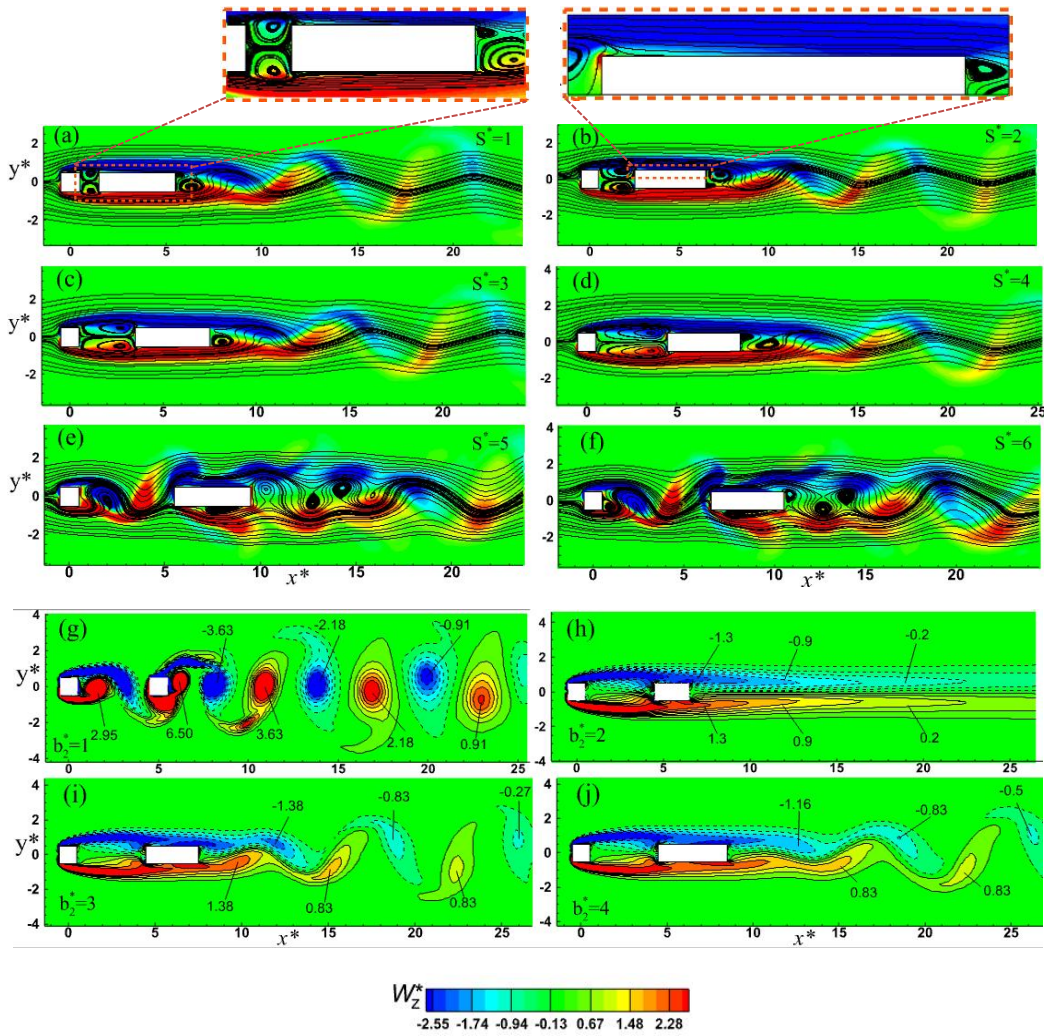


Figure 6. (a-f) Instantaneous streamlines colored with vorticity for various S^* at $b_2^* = 4$ (g-j) instantaneous vorticity for different $b_2^* = 1-4$ at $S^* = 4$ ($Re = 150$ and $b_1^* = 1$).

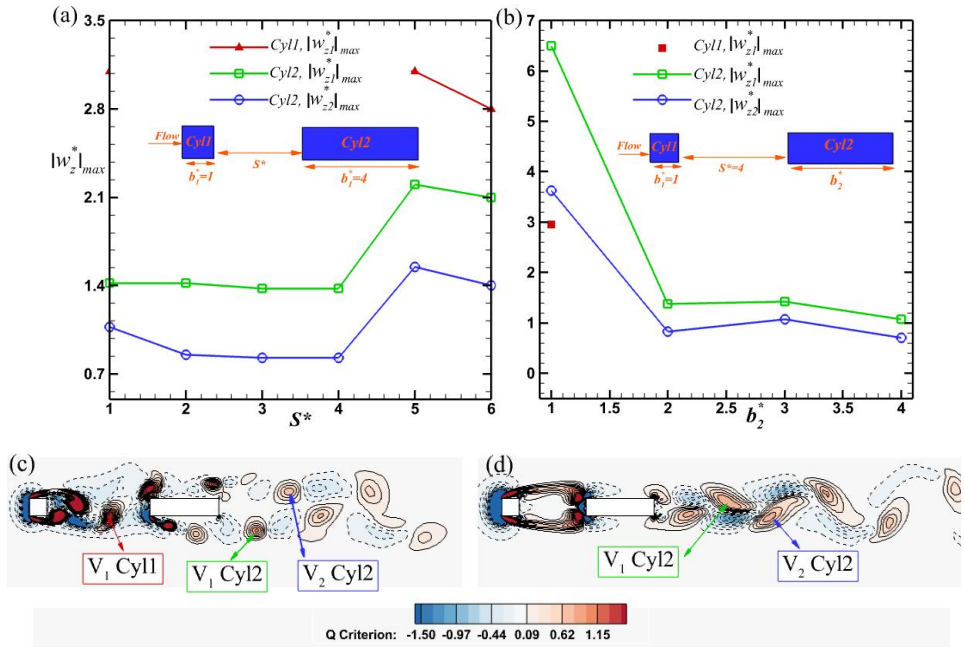


Figure 7. The maximum vorticity magnitude for various (a) S^* ($Re = 150, b_2^* = 4$) and (b) b_2^* ($Re=170, S^*=4$), $|w_z^*|_{max}$. The detached vortices identified with the Q criterion behind the upstream and downstream cylinders discussed in (a, b) have been marked in subplots c (CSF) and d (EBF).

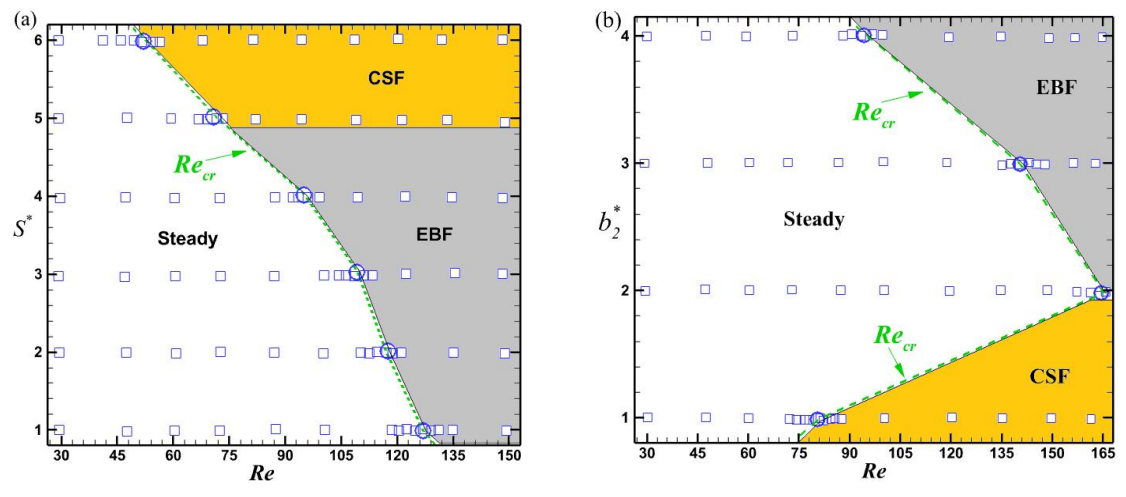


Figure 8. View of all simulations performed (a) for various S^* and Re ($b_1^* = 1, b_2^* = 4$), (b) for various b_2^* and Re ($b_1^* = 1, S^* = 4$), wherein these flow maps EBF and CSF stand for extended-body flow and co-shedding flow, respectively.

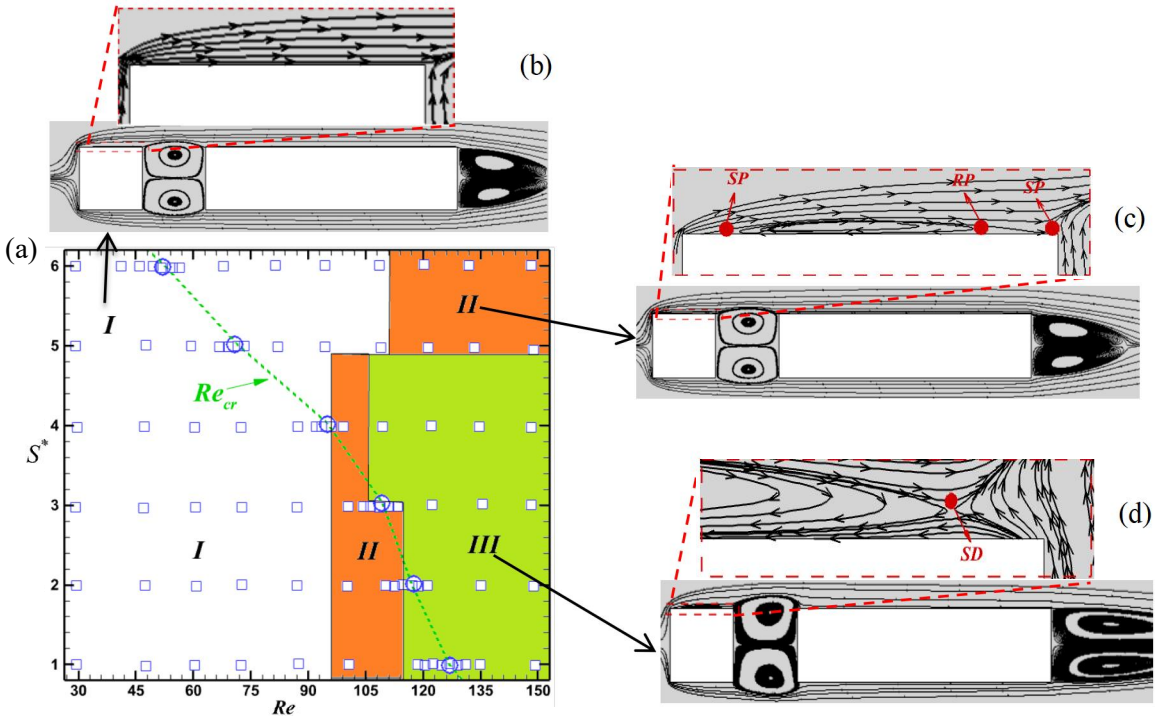


Figure 9. (a) Marginal time-mean flow map at S^*-Re plane. The simulated cases with $b_1^* = 1$, $b_2^* = 4$, at a wide range of S^* and Re in the present study have been marked with a blue hollow square. The green dashed line with a hollow circle indicates Re_{cr} . The mean streamlines of the three time-mean flows are shown for patterns (b) I (white background in (a)), (c) II (orange background in (a)), (d) III (green background in (a)). SP: Separation point, RP: Reattachment point, SD: Saddle point.

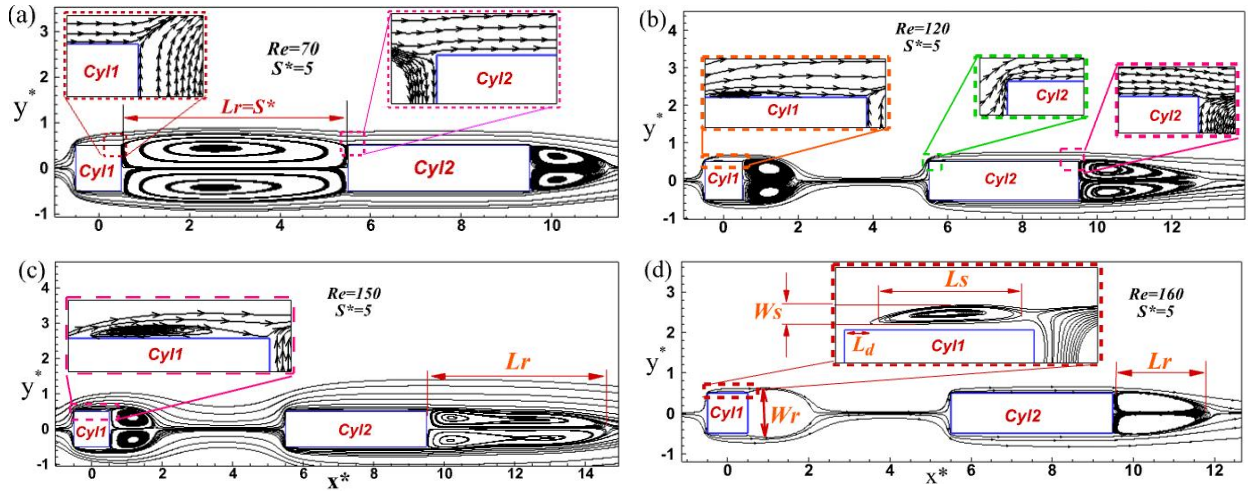


Figure 10. Mean flow (a) pattern I, (b, c) pattern II and (d) pattern III ($b_1^* = 1$, $b_2^* = 4$, $S^* = 5$ and $Re = 70-150$). The parameters of L_r , W_r , L_s , W_s , and L_d are shown in (a, d).

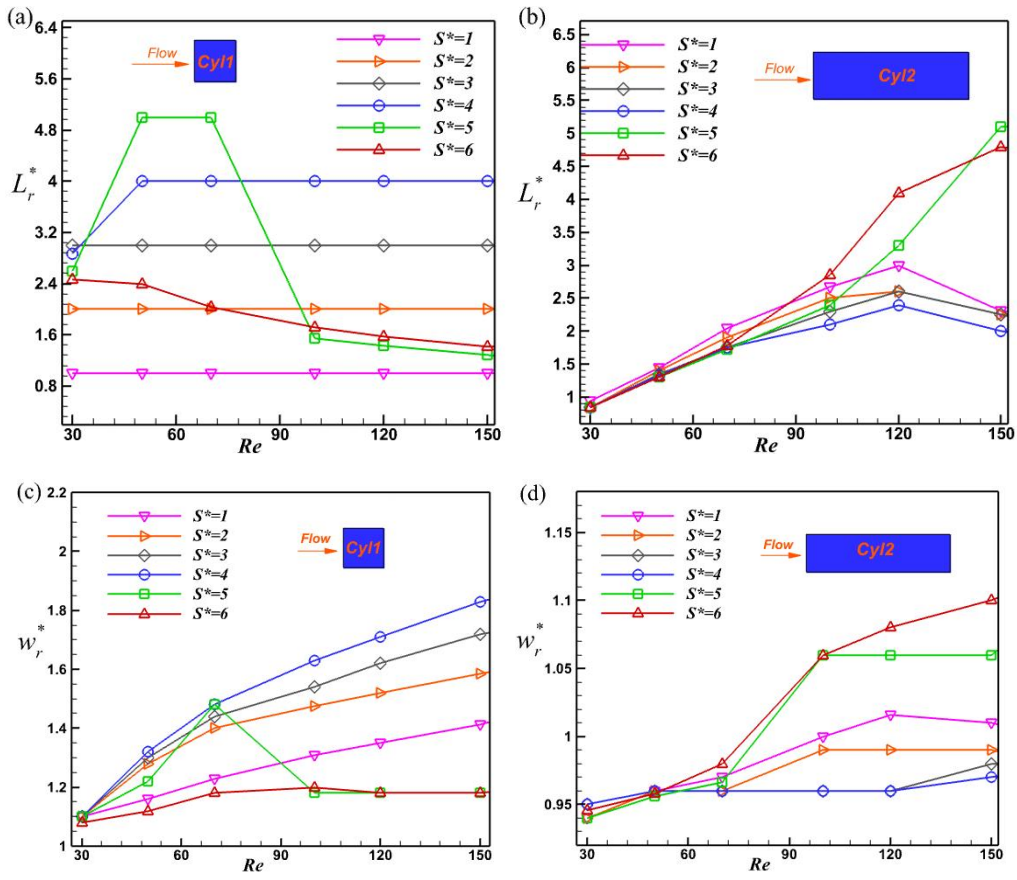


Figure 11. (a, b) the bubble length L_r^* , and (c, d) bubble width W_r^* for both cylinders at various Re and S^* ($b_2^* = 4$), see also Fig. 10(a, d).

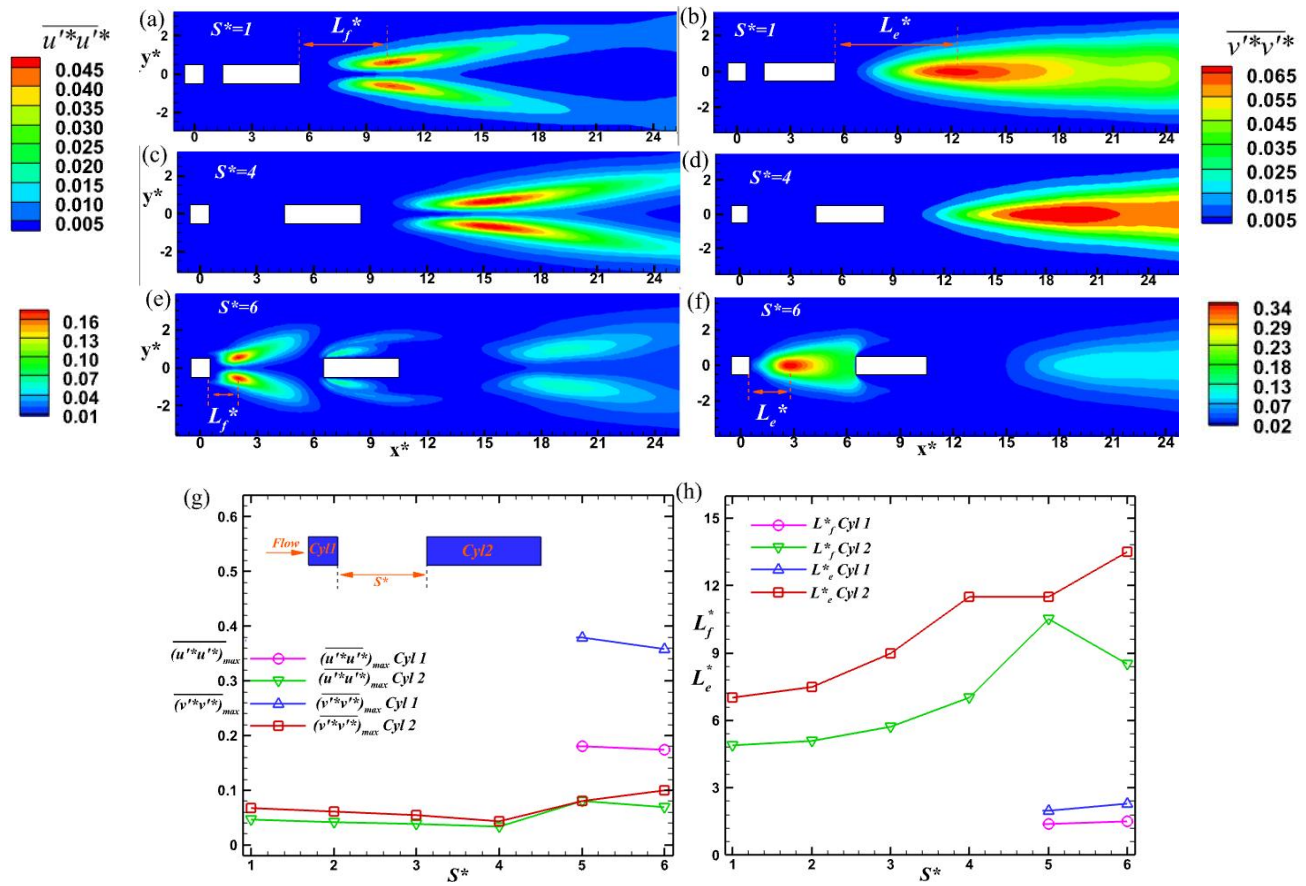


Figure 12. (a, c, e) The $\overline{(\mathbf{u}^* \mathbf{u}^*)}$ and (b, d, f) $\overline{(\mathbf{v}^* \mathbf{v}^*)}$ contours for various S^* . (g) The variation of maximum values, i.e., $\overline{(\mathbf{u}^* \mathbf{u}^*)}_{\max}$ and $\overline{(\mathbf{v}^* \mathbf{v}^*)}_{\max}$ (h) L_e^* and L_f^* with S^* ($b_1^* = 1$, $b_2^* = 4$, and $Re = 150$).

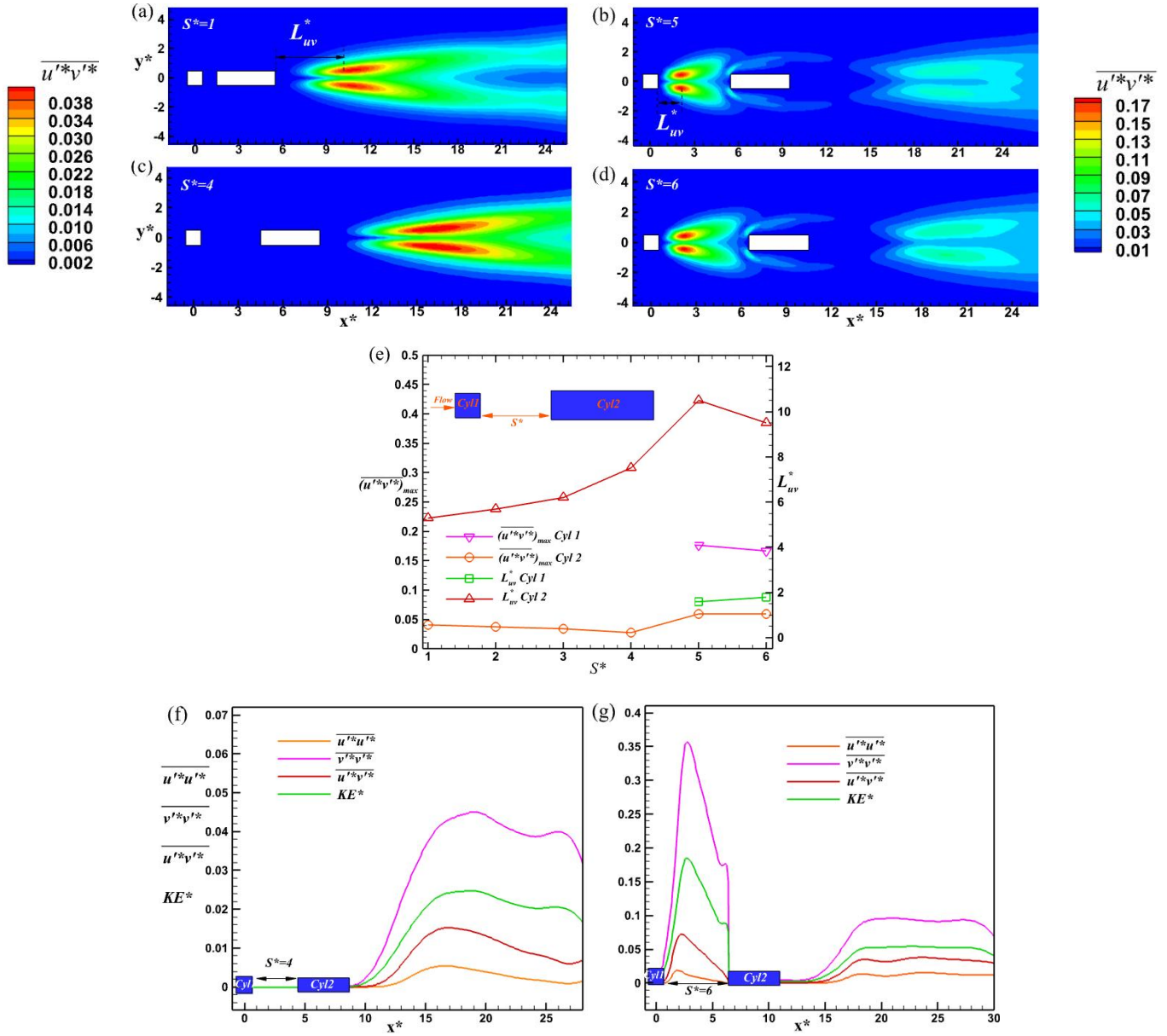


Figure 13. (a-d) The $\overline{u^*v^*}$ contours for various S^* , (e) the variations of $(\overline{u^*v^*})_{\max}$ and L_{uv}^* with S^* , the variations of KE^* , $(\overline{u^*u^*})$, $(\overline{v^*v^*})$ and $(\overline{u^*v^*})$ on the center line of the cylinders ($y = 0$) (f) $S^* = 4$, (g) $S^* = 6$, ($\mathbf{b}_1^* = 1$, $\mathbf{b}_2^* = 4$ and $Re = 150$).

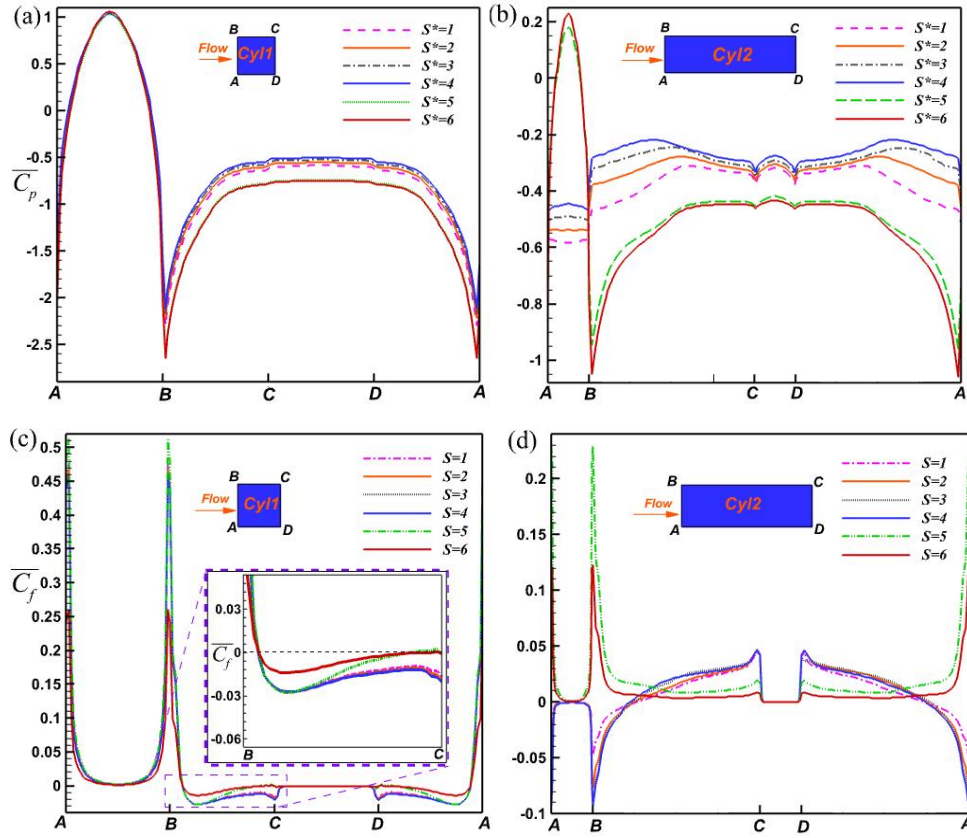


Figure 14. (a,b) Time-mean local pressure coefficient (\bar{C}_p) and (c,d) local friction coefficient (\bar{C}_f) for (a, c) upstream cylinder ($b_1^* = 1$) and (b, d) downstream cylinder ($b_2^* = 4$), $S^* = 1-6$ and $Re = 150$.

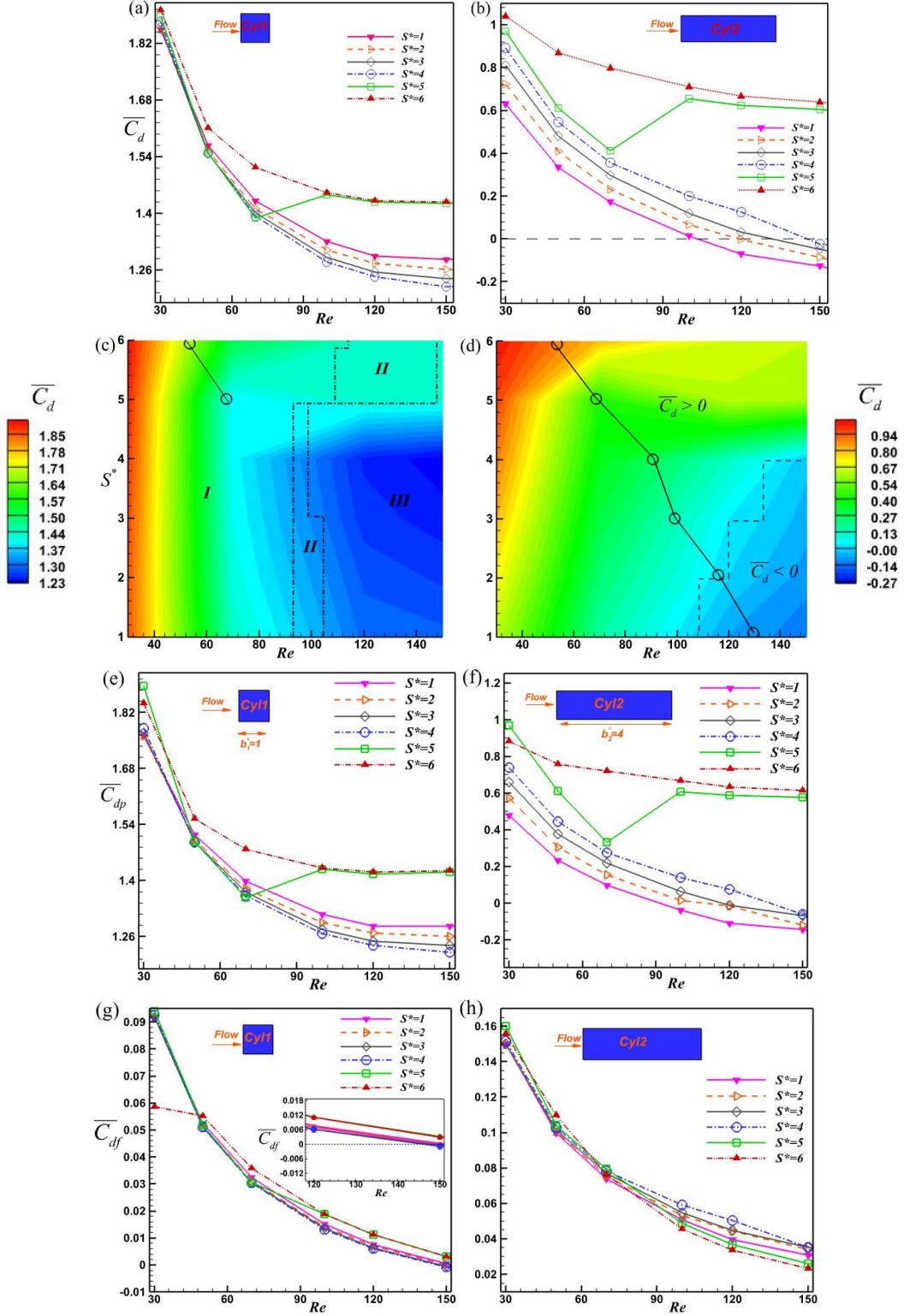


Figure 15. The profiles and contours of total drag coefficients, pressure drag coefficients profiles (e, f) friction drag coefficients profiles (g, h) for various Re and S^* and both cylinders. Upstream cylinder ($b_1^* = 1$, plots a, c, e, g) and downstream cylinder ($b_2^* = 4$, plots b, d, f, h). In the contours line with a circle, dashed lines, and long-dashed lines indicate Re_{cr} , the boundary between three mean flow patterns, and the boundary between positive and negative drags coefficient, respectively.

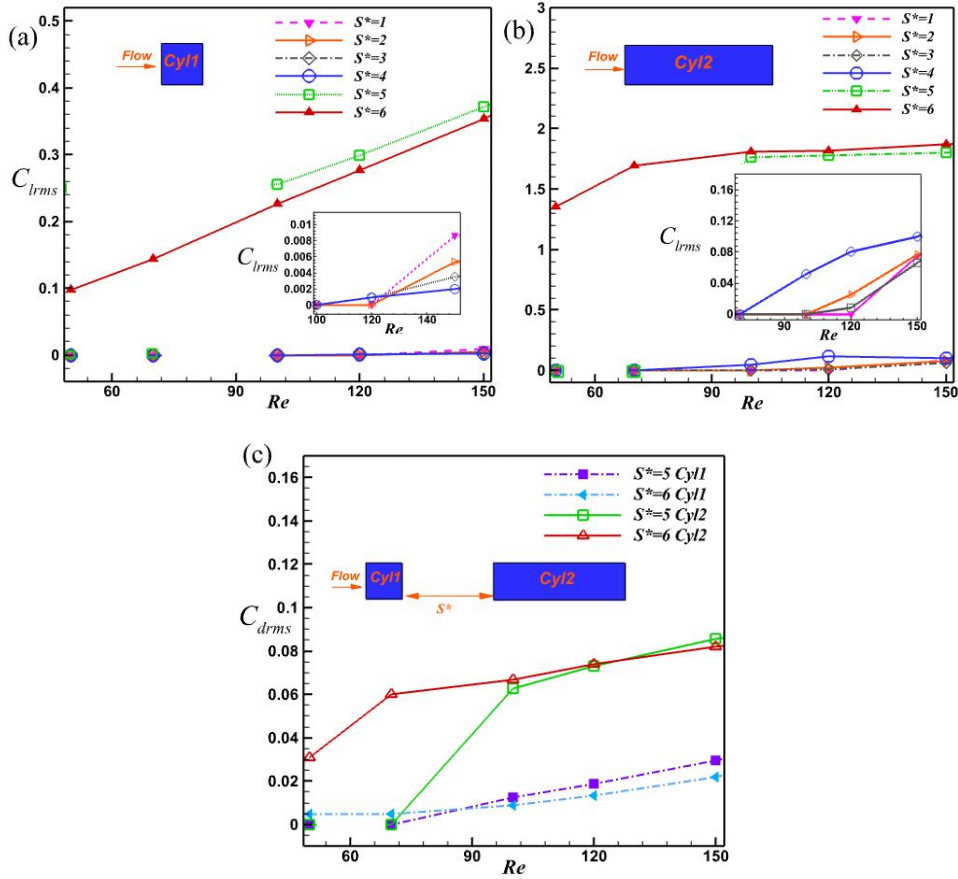


Figure 16. Variations of the C_{lrms} and C_{drms} for various Re and S^* (a) C_{lrms} for upstream cylinder ($b_1^* = 1$), (b) C_{lrms} for the downstream ($b_2^* = 4$) and (c) C_{drms} for both cylinders.

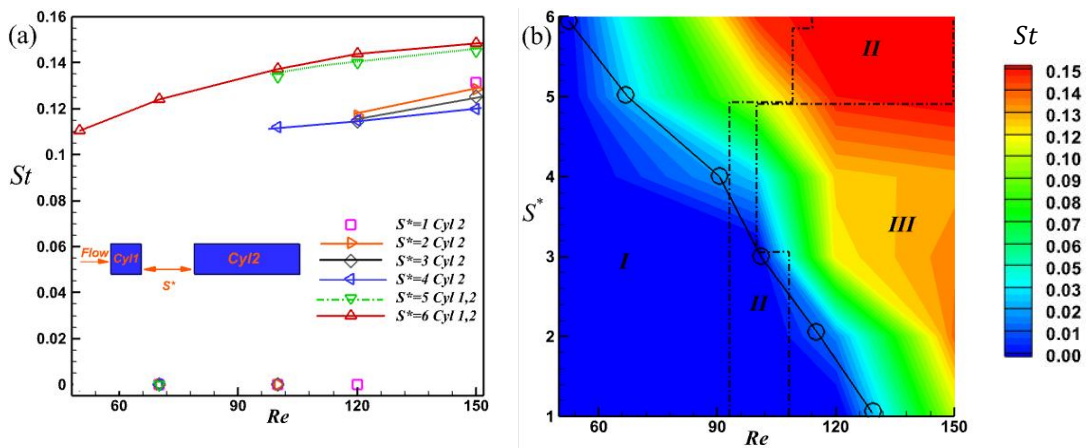


Figure 17. Variations of St versus Re and S^* ($b_1^* = 1$, $b_2^* = 4$) in (a) profiles and (b) contour. The line with circle and dashed dot lines respectively indicate Re_{cr} and the time-mean flow boundaries in the contour.

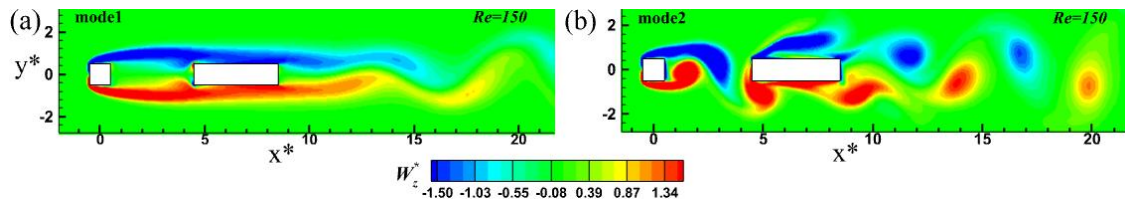


Figure 18. Vorticity contours for two tandem cylinders ($b_1^* = 1$, $b_2^* = 4$) at $Re = 150$ and $S^* = 4$ (a) Mode 1 (extended-body flow pattern or EBF), (b) Mode 2 (co-shedding flow pattern or CSF).

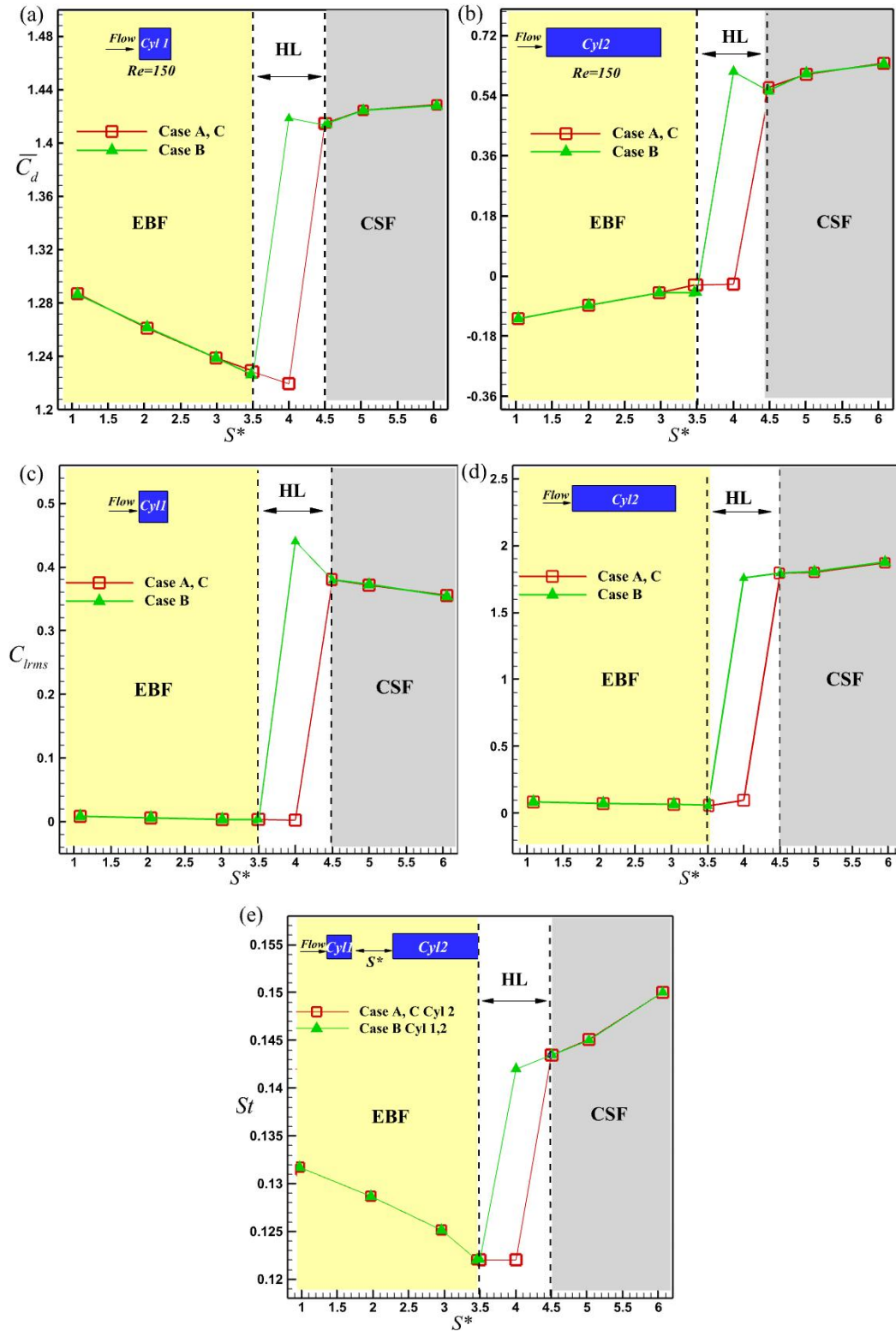


Figure 19. The variation of (a, b) \bar{C}_d , (c, d) $C_{l_{rms}}$ and (e) St ($b_1^* = 1$, $b_2^* = 4$) at $Re = 150$. EBF; extended-body flow pattern, HL; hysteresis limit, CSF; co-shedding flow pattern.

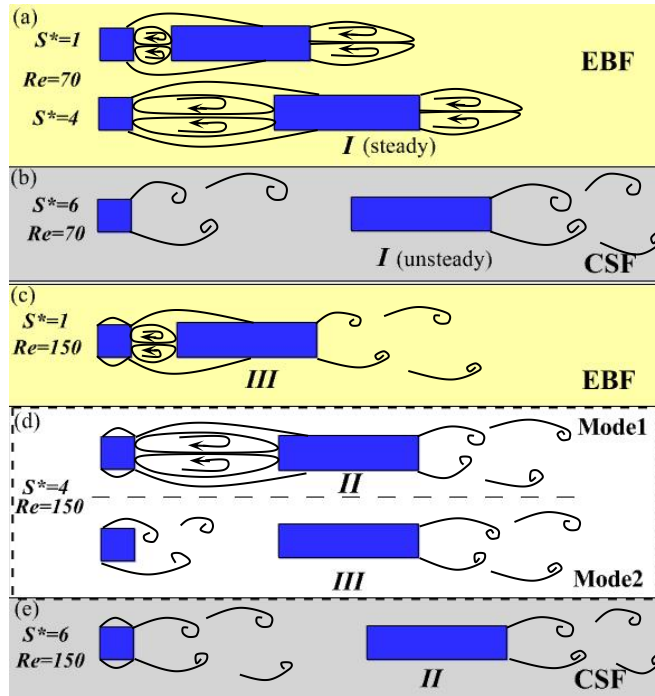


Figure 20. Overview of the flow patterns depends on S^* and Re ($b_1^* = 1, b_2^* = 4$). EBF: extended-body flow pattern, CSF: co-shedding flow pattern.